Optimizing the Antibacterial Activity of Iron Oxide Nanoparticles Using Central Composite Design

Mohammed Laid Tedjani[1,3] · Abdelhamid Khelef[2,3] · Salah Eddine Laouini[1,3] · Abderrhmane Bouafia[1,3] · Norah Albalawi[4]

Abstract

This work aims to optimize the antibacterial activity of iron oxide nanoparticles (IONPs) against both Gram-positive and Gram-negative bacteria. IONPs were greenly biosynthesized using *Moringa oleifera* leaves extract, and surface methodology (RSM) based on central composite design (CCD) was employed to investigate the combined effect of various experimental factors on the antibacterial activity of IONPs. The reaction and annealing temperatures besides precursor concentration were set as independent variables, while the antibacterial activity was set as a response to obtain the optimal conditions that maximizes IONPs antibacterial activity. Different characterization techniques such as UV–Vis, FTIR, XRD, SEM, and EDX were employed to study the properties of the biosynthesized nanoparticles. Meanwhile, the antibacterial activity was tested using the disk diffusion method. The characterizations results have confirmed the biosynthesis of Hematite (α-Fe_2O_3) nanoparticles of rhombohedral structure. The generated model has exhibited predicted values very close to the actual proving its validity to analyze and optimize the studied process. The model indicated that all the investigated parameters and their interactions have significantly affected IONPs antibacterial activity. An optimal antibacterial activity was achieved when biosynthesis factors at their lower levels (-1). Furthermore, the effect of IONPs size on the antibacterial activity was studied and the results shown that the latter is significantly related to the nanoparticles size.

✉ Mohammed Laid Tedjani
   medlaidtedjani@gmail.com

1   Department of Process Engineering and Petrochemistry, Faculty of Technology, University of Echahid Hamma Lakhdar El Oued, 39000 El-Oued, Algeria

2   Department of Chemistry, Faculty of Exact Sciences, University of Echahid Hamma Lakhdar El Oued, 39000 El Oued, Algeria

3   Lab, VTRS, Faculty of Technology, University in El Oued, 39000 El Oued, Algeria

4   School of Chemistry and Molecular Biosciences, The University of Queensland, Brisbane, Australia

Graphical Abstract
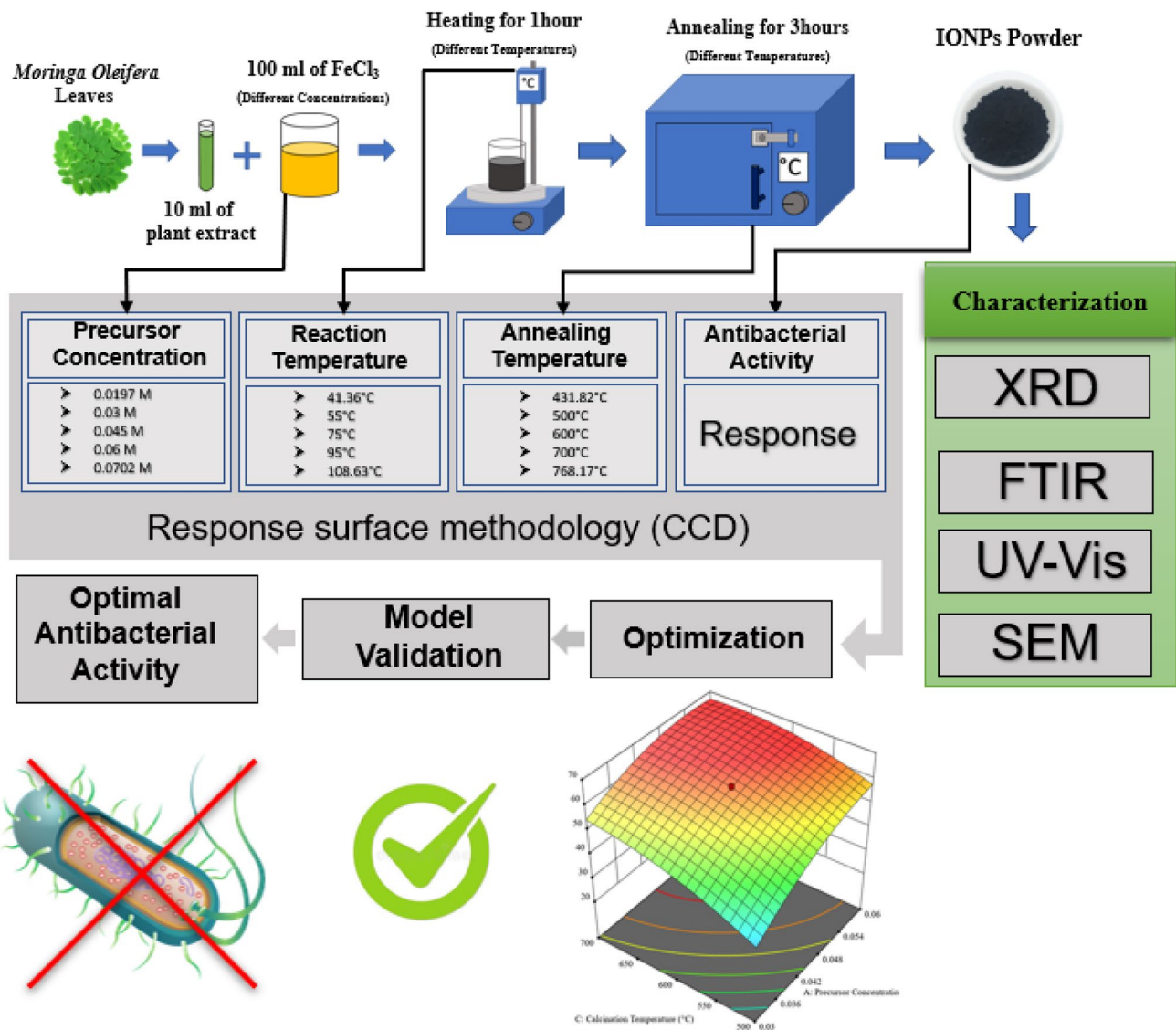
Abbreviations

Pre-Con	Precursor concentration
RC Temp	Reaction temperature
ANL Temp	Annealing temperature
IONPs	Iron oxide nanoparticles
RSM	Response surface methodology
M. olivera	*M. oleifera*
CCD	Central composite design
E. coli	*Escherichia coli*
S. aurus	*Staphylococcus aureus*
ANOVA	Analysis of variance
NPs	Nanoparticles

1 Introduction

In the past two decades, nanoscale materials of single or multidimensions and a size below 100 nm have attracted increasing interest due to their new and unique features over their bulk counterparts [1]. The new features of these materials have made revolutionary improvements in many fields,

making nanoscience one of the most promising and innovative fields of research in materials sciences.

Various inorganic materials have been modified, and their size was reduced to nanoscale as nanoparticles to achieve superior properties with greater functional versatility. Among the inorganic nanoparticles, Iron oxide nanoparticles (IONPs) in particular magnetite (Fe_3O_4), maghemite (γ-Fe_2O_3), and hematite (α-Fe_2O_3) are of great technological and industrial interest due to their unique properties appropriate for many fields, including the electronics industry for the fabrications of the new generation technological devices [2], the agriculture sector as a fertilizers [3], environmental remediation removal of pollution or contaminants from water [4], and the various applications in medicine field [5, 6].

Among the different applications in medical field, metal nanoparticles have been extensively explored to combat one of the leading causes of death in worldwide known as the infections of pathogenic bacteria [7–13]. Bacteria are continuously developing resistance towards different antibiotics, which have arisen the necessary of discovering a new antibacterial agent class [14]. The recent studies concerning inorganic nanomaterials have proven their efficiency as antibacterial agents against many bacterial infections they can be used to enhance the effectivity of existing antibiotics or used directly as antibacterial agent since they exhibit antibacterial features of their own [15, 16].

There are three proposed antibacterial mechanisms of IONPs against bacterial cells. The first mechanism suggests that IONPs enable the formation of reactive oxygen species (ROS) such as hydroxyl ions and hydrogen peroxide, which causes oxidative stress and damages the cell membrane and DNA, leading to bacterial death [17]. The second mechanism by the dissolution of IONPs into iron ions, which is known to inhibit several bacterial cells activities by interfering with enzyme, amino acid, and protein metabolisms causing bacterial death [18]; and the third mechanism propose that IONPs interact directly with cell membrane through electrostatic forces, which damages the membrane plasma, and causes intracellular content leaks [19].

Diverse chemical and physical processes have been extensively employed for the fabrication of metal nanoparticles. However, these production methods are generally costly, toxic, and potentially dangerous to the environment and living organisms. Which have arisen many concerns about the production of nanomaterials; these concerns are faded by implementing a sustainable green biological method in nanomaterials production, which uses biodegradable and biocompatible natural sources such as bacteria fungi, and plant extracts. This synthesis method allowed the production of low-cost, non-toxic, and eco-friendly nanomaterials [20].

The unique features of iron oxide nanoparticles including their antibacterial activity are significantly influenced by their shape and size [2, 21–26]. Generally, significant enhancements on nanoparticles properties are reached by reducing their size. Therefore, extensive studies and efforts were made to better understand the relationship between the size and properties, aiming to reach a size-controlled synthesis of nanoparticles with optimized properties and best performance [27].

Former studies in the literature have found that it is possible to control nanoparticles' size and properties by adjusting the synthesis conditions including reaction temperature, pH, duration, and reactant concentration that significantly influences the growth of nanoparticles' crystallite size [28–33].

The majority of the former investigations aiming to optimize the nanoparticles antibacterial activity have restricted their examinations to study the influence of only discrete or separate synthesis parameters with a primitive technique widely known as one factor at time (OFAT) optimization. This technique is surrounded by various disadvantages that restricted employing it to solve real industrial problems, it needs a non-reasonable number of tests that can be extremely costly and consumes a lot of resources efforts and especially time. On top of that, its unable to describe the interactive effect of multiple synthesis factors [34].

The prementioned complications can be effectively and efficiently diminished using modern and effective statistical techniques that permit the investigation and the modelling of multiple independent variables. Response surface methodology (RSM), is considered as one of the most powerful and efficient techniques used for this purpose. This technique consisted of generating a polynomial equation that can simulate the experimental data and predict processes output by linking the effect of the studied variables and their response with a mathematical model.

The generated mathematical model is exploited to assist determining the optimal conditions of any process maintaining a reasonable number of experiments, consequently less efforts, recourses and time [35–37].

Moringa oleifera or *Drumstick* tree is one of the world's most beneficial and easily accessible trees. It is the only genus among fourteen species of the *Moringaceae* family. *Moringa* has an extensive geographic distribution throughout Central and South America, Africa, and South Asia due to its capability to quickly grow and resistance to poor soil [38]. Besides using it as food, *M. oleifera* is also famous for its important healing abilities which make it earn the name of "the miracle tree" or "the tree of life" [39]. It

is rich in flavonoids, phenolic acids, phenolic amines, vitamins, protein, and minerals [40].

This paper aims to optimize the antibacterial activity of IONPs against both Gram-positive and Gram-negative bacteria. IONPs were greenly biosynthesized using *M. oleifera* leaves extract, then, dissimilar to the limited traditional one factor at time (OFAT) optimization studies, we have investigated the collective effect of various experimental factors on the antibacterial activity of IONPs. The reaction and annealing temperatures besides precursor concentration were set as independent variables and were varied in a broad range of five levels for each variable, while the antibacterial activity was set as a response to obtain the optimal conditions that maximize IONPs antibacterial activity. To the best of our knowledge, there is no study have been conducted examining the interactive effect of this combination of factors on antibacterial activity of IONPs. In order to study the properties of the biosynthesized nanoparticles, different characterization techniques such as UV–Vis, FTIR, XRD, SEM, and EDX. Meanwhile, their antibacterial activity was tested using the disk diffusion method.

Table 1 Information about the collection of *M. oleifera*

Location	Site name	Geographical coordinates	Altitude (m)	Bioclimatic zone	Collection date
El-Oued, Algeria	Bagouza	Latitude: 33°,49 N Longitude: 06°,72 E	68	Arid	12/10/2019

2 Materials and Methods

2.1 Chemicals

Analytical grade Ferric chloride (FeCl$_3$ 98%) purchased from Sigma Aldrich, and Milli-Q water were used in all the performed trials.

2.2 Sample Collection and Preparation of *M. oleifera* Plant Extract

2.2.1 Sample Collection

Moringa oleifera leaves were gathered from a local farm in Bagouza, Taghzout, 20 km from the provincial capital, El Oued. The leaves were collected on the 12th of October 2019. Additional information about the collection of *M. oleifera* is shown in Table 1 and Fig. 1.

2.2.2 The Preparation of Plant Extract

First the green leaves were washed deeply with Deionized water and then left to dry away from sunlight for two weeks at room temperature. The leaves mixed continuously enabling the air to pass through the leaves. After that, electronic grinder was used to crush the air-dried leaves and then using the obtained fine powder to prepare the plant extract utilizing the maceration method [41, 42]; 10 g of plant powder was added to 100 mL of deionized water and mixed steadily over night at room temperature. Finally, the liquid phase was
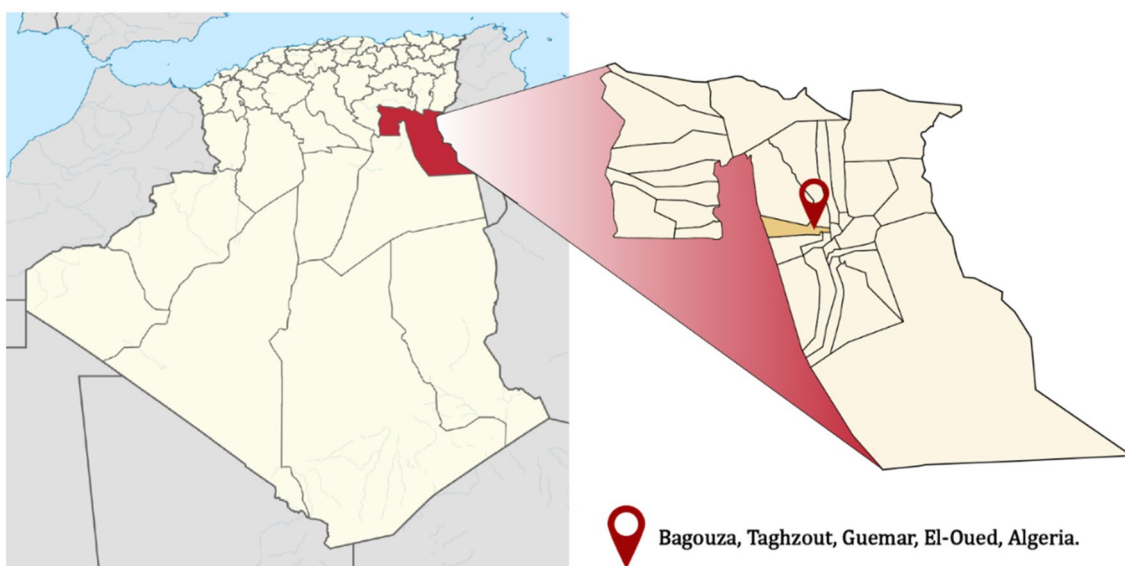
Fig. 1 Geographic map showing the collection area

separated with Whatman No.42 filter paper several times and then stored in a refrigerator at 4 °C for further use.

2.3 The Biosynthesis of Iron Oxide NPs

IONPs biosynthesis was performed with minor modifications to a standard method used by prior studies for the plant mediated synthesis of metal oxide NPs [43, 44]. First, 10 mL of *M. oleifera* leaves extract was poured into 100 mL of different concentrations of iron chloride solutions (0.02–0.07 M). This combination left to react under various temperatures (from 55 to 95) for one hour and magnetic stirring rate of 350 rpm. A sample from each resulted solution was conserved for UV–Visible analysis. Next, the resulting mixture was centrifuged for 15 min with a rate of 3000 rpm, and the precipitated solid was washed with deionized water several times and dried in air-oven at 50 °C overnight. Finally, the dried solid of the different samples was annealed for 3 h at different temperatures (430–768 °C) in order to purify the synthesized nanoparticles by removing the impurities and to ensure their full crystallization [45–47]. Schematic illustration of the IONPs biosynthesis method is shown in Fig. 2.

2.4 Characterization of Iron Oxide Nanoparticles

The UV–visible spectrum of IONPs was recorded using a double-beam UV–Visible spectrophotometer (Shimadzu 1800) recording the range of 200–900 nm. Before the analysis, IONPs solution concentration was reduced by pouring 1 mL of the obtained iron oxide NPs solution in 10 mL of Milli-Q water. Quartz cuvette was used in this analysis, and distilled water was used as the reference solvent. FTIR spectra were recorded on total reflection (ATR) spectrometer (Thermo scientific-Nicolet iS5) operating in the range of 400–4000 cm^{-1}. The XRD patterns were recorded using

X ray diffractometer (Rigaku, Mini Flex 600) operating in 2θ range from 20° to 80° with Kα radiation of copper ($\lambda = 1.5406$ Å). The X rays were produced with 30 kilovolts and current intensity of 20 mA. The iron oxide NPs at the optimal conditions were imaged using (FEI, QUANTA-250 FEG) microscope operating under a voltage of 20 Kilovolts and high vacuum and Scherrer formula (Eq. 1), was used to estimate the crystallite size by choosing the peak with the highest intensity assigned to the plane (104).

$$D = \frac{k\lambda}{\beta \cos \theta} \qquad (1)$$

D signifies the crystallite size, k denotes the shape factor, β is FWHM (the full width at half maximum), λ is the wavelength (1.5418 Å, Cu$K\alpha$) and θ is the so-called diffraction angle [48].

2.5 Antibacterial Activity

The antibacterial activity of the biosynthesized IONPs was investigated using the disk diffusion method. Before the experiment, pure cultures of two human pathogens, *E. coli* and *S. aureus*, were isolated from patient's samples collected from (Abd El-hakim) Laboratory, Boudouaou, Algeria and (El-Medjed) Laboratory, El-Oued, Algeria. The bacteria were then sub cultured on nutrient agar (NA) and incubated at a temperature of 37 °C overnight.

Different runs of IONPs of different sizes were properly sonicated and dispersed in deionized water in concentrations of 50 mg/mL. The dispersed IONPs were loaded to 7 mm disks made of No.1 Whatman filter paper.

Mueller–Hinton agar (MHA) was heated to 55 °C, then 20 mL from the solution was poured in a petri dish and left to solidify for 15 min; the preprepared bacteria then was dispersed in saline solution (NaCl 0.9%) using a vortex

Fig. 2 Schematic illustration of the IONPs biosynthesis method
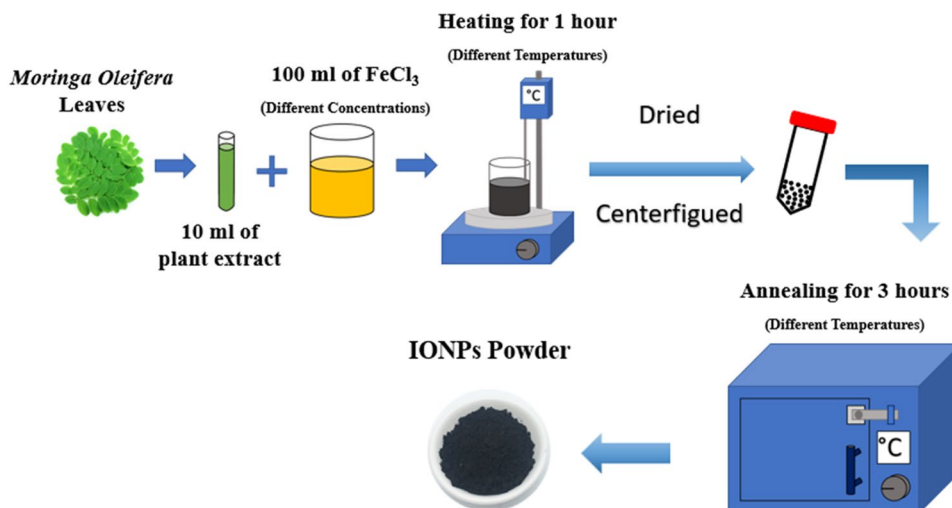
mixer (2550 rpm) in microorganism concentration of 0.5 McFarland. After that, the bacterial uniformly dispersed at the MHA surface using cotton swab.

The different runs of IONPs of various sizes were properly sonicated and dispersed in deionized water in concentrations of 50 mg/mL. Then, the dispersed IONPs were loaded to 7 mm disks made of No.1 Whatman filter paper. Gentamycin (120 mg/mL) was used as a positive control, while deionized water was the negative control.

Finally, the prepared IONPs disks along with positive and negative controls were placed at the MHA surface at 37 °C for 24 h. At the end of incubation, inhibition zones formed around the disc were measured with a transparent ruler in millimeters.

2.6 Experimental Design

Box-Wilson Central Composite Design, frequently known as central composite design (CCD) was used in this study due to proficiency in generating response surfaces that can be employed to predict the optimal desired response with fewer number of runs. CCD is a two-level factorial design, improved with center and star points that enables fitting the quadratic polynomial models [49]. In this design the independent variables (inputs) are wide-ranging over 05 levels: the high level (1), lower level (-1), center points (0), added to 02 outer (star) points symbolized (α and $-\alpha$). that signify the extreme levels for each factor. For a rotatable design having m factors, $\alpha = 2^{m/4}$. In the design used for this study $m = 3$ so $\alpha = 2^{3/4} = 1.682$.

The choice of suitable ranges for the studied factors was inspired from the previous studies. It was reported that the ANL Temp of 500 °C synthesizes a clean IONPs [43, 44, 50]. Therefor 500 °C was selected as the low level (-1) for this factor. Moreover, According to former studies, the recommended reaction temperature (RC Temp) for the biosynthesis of the metallic oxide nanoparticles using plant extracts is in the range of 25–100 °C [51]. Consequently, 95 °C was chosen as the high level (1) for RC Temp parameter. The PR Con ranged from 0.03 to 0.07 in order to be suitable for the volume of the plant extract used in this biosynthesis process [28, 52]. Table 2 shows the coded and real values of the levels of each independent variable.

The total reduced number of the runs required for this study according to CCD can be calculated using Eq. (2).

$$N = 2^n + 2n + n_c \tag{2}$$

where N is the entire number of experimental runs, n is the number of independent variables (Three in our case). 2^n, $2n$ and n_c are assigned to factorial, axial and center runs respectively. For aquert error calculations the number of center points recommended for three variables is six [53]. Therefore, for this study taking $n_c = 6$ and $n = 3$ the total number of runs needed is 20 according to Eq. (2). The performed runs are listed with their actual values in Table 3.

In central composite design that contains 03 factors, the quadratic model can be expressed as follows (3):

$$Y = \beta_0 + \sum_{j=1}^{m} \beta_j x_j + \sum_{j=1}^{m} \beta_{jj} x_j^2 + \sum \sum_{i<j=2}^{m} \beta_{ij} x_i x_j + \varepsilon \tag{3}$$

where x_i and x_j are factors (i and j varies from 1 to m). ε represents the error. The coefficients β_i, β_{ii}, and β_{ij} represent the linear, binominal and combined effects, respectively. β_0 is a constant coefficient, m signify the sum of studied factors [54, 55].

2.7 Data Analyses

Design expert (version 13) statistical software was employed for the construction of the experimental design and analyzing the obtained data by generating the different statistical reports and plots, investigating the different effects of the chosen variables, and determining the optimal conditions within the studied range.

3 Results and Discussions

The formation IONPs was clearly distinguished by the immediate color change from light brown to dark black.

Figure 3 when the ferric chloride (FeCl₃) solution was mixed with *M. oleifera* leaves extract which was clearly noted by naked eye observation. This result match those observed in earlier studies using diverse plants [2, 3]. The color change occurred due to the presence of the active molecules in the used extract, which reduced the iron metal ions.

M. oleifera is a rich source of biomolecules such as (polyphenols, flavonoids, terpenoids, alkaloids, tannins, etc.) that can reduce and stabilize metal ions to their nano form. When

Table 2 The different levels and codes of the studied factors

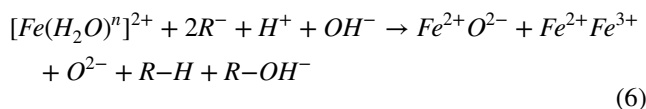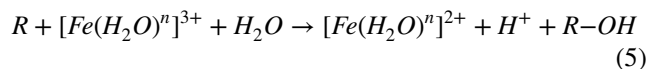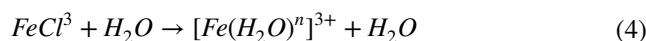| Factors	Codes	Levels				
		$-\alpha$	-1	0	$+1$	$+\alpha$
PR Con (M)	A	0.02	0.03	0.045	0.06	0.07
RC temperature (°C)	B	41	55	75	95	108
ANL temp (°C)	C	431	500	600	700	768

Table 3 Experimental design plan for the three factors with the observed responses

Run	Actual values			Inhibition zone (nm)			
	A	B	C	Experimental		Predicted	
	PR Con	RC Temp	ANL Temp	E. coli	S. aureus	E. coli	S. aureus
1	0	0	0	13.4	12.7	13.76	12.56
2	0	0	0	14.7	12.8	13.76	12.56
3	0	0	−1.682	21.6	17.8	21.10	18.14
4	0	0	1.682	12.7	10.6	13.40	10.58
5	1	1	1	22.8	20	22.95	20.07
6	0	0	0	13.3	12	13.76	12.56
7	0	0	0	13.8	13	13.76	12.56
8	1.682	0	0	13	11	13.30	11.62
9	−1.682	0	0	21.8	19.3	21.70	19.00
10	0	1.682	0	16.7	14	16.61	14.42
11	1	−1	1	14.5	12.6	13.98	12.43
12	0	0	0	13.4	12.3	13.76	12.56
13	1	1	1	12.5	10	12.21	9.71
14	1	1	−1	15.8	13.7	15.94	13.16
15	−1	1	−1	22	19.9	22.38	19.84
16	−1	1	1	18	15.4	17.80	15.40
17	−1	−1	1	17.8	14.2	17.52	14.52
18	1	−1	−1	18.5	17.2	18.56	16.98
19	0	0	0	14	12.6	13.76	12.56
20	0	−1.682	0	18.3	17	18.58	16.90
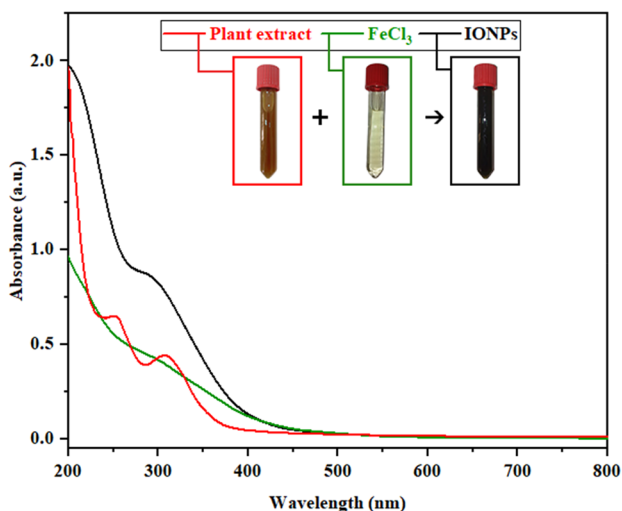
Fig. 3 UV–vis absorbance spectra of IONPs and the plant extract

ferric chloride salt (FeCl$_3$) dissolves in water, it forms an ionic solution of iron and chlorine ions that moves freely moves in the solution. Once the ionic solution is mixed with *M. oleifera* liquid extract, the freely moving iron ions are attracted towards the plant's biomolecules due to electron deficiency. This leads to transferring electrons from oxygen to iron ions according to the donor–acceptor mechanism

causing the reduction of iron ions to zero-valent NPs. This latter is then stabilized by the other biomolecules of the plant extract. On the other side, the plant biomolecules are converted to keto compounds. The reduced iron nanoparticles are transformed into iron oxide nanoparticles during air-drying and annealing [1]. The bioreduction process can be induced as follows:

$$FeCl^3 + H_2O \rightarrow [Fe(H_2O)^n]^{3+} + H_2O \tag{4}$$

$$R + [Fe(H_2O)^n]^{3+} + H_2O \rightarrow [Fe(H_2O)^n]^{2+} + H^+ + R-OH \tag{5}$$

$$[Fe(H_2O)^n]^{2+} + 2R^- + H^+ + OH^- \rightarrow Fe^{2+}O^{2-} + Fe^{2+}Fe^{3+}$$
$$+ O^{2-} + R-H + R-OH^- \tag{6}$$

The UV visible graphs corresponding to IONPS and *Moringa* leaves extract are shown in Fig. 3. Two peaks located around 250 and 320 nm appeared in the plant extract spectrum. Meanwhile, IONPs spectrum exhibited a single peak at 275 nm. This peak is attributed to the characteristic IONPs SPR Surface Plasmon Resonance absorption band of [50, 56, 57].

The gap energy E_g of the synthesized IONPs was determined from the UV–Visible spectrum. Figures 4 and 5 shows the variation of ($\alpha h v$) as a function of ($h v$) the gap
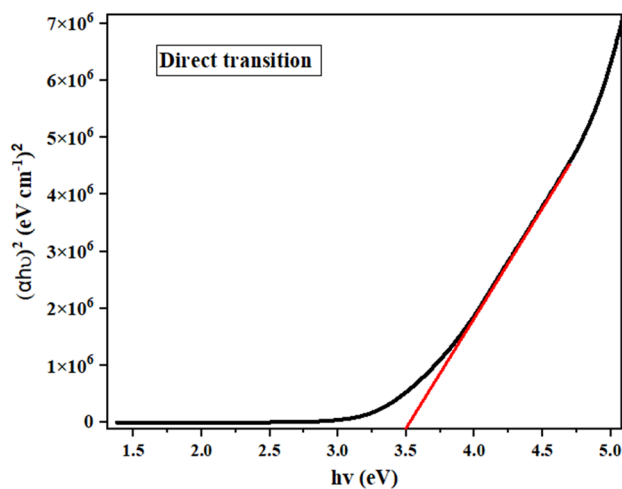
Fig. 4 Direct bandgap (Eg) estimation using Tauc's plot

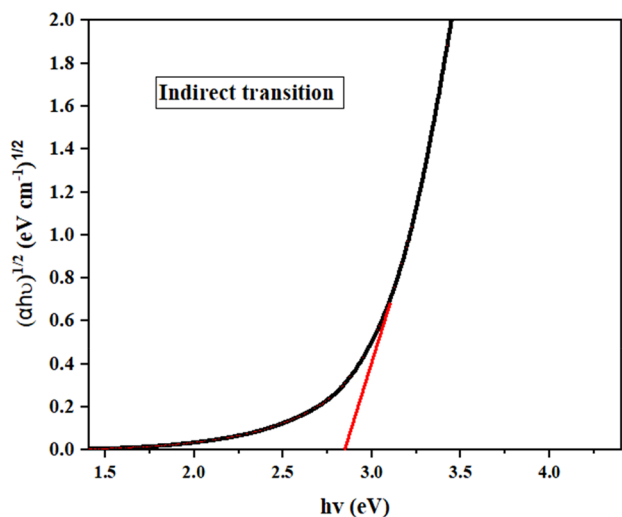**Fig. 5** Indirect bandgap (Eg) estimation using Tauc's plot

energy (E_g) of nanoparticles is estimated using Tauc's formula (Eq. 7) [58]:

$$(\alpha h\upsilon) = K(h\upsilon - E_g)^n \tag{7}$$

K is a constant and $h\upsilon$ represents the energy of the incident photon. α the absorption coefficient. E_g the optical band gap in electron volts (eV). n is an variable exponent that depends on the nature of the electronic transition (when the transition is direct $n = 2$, and when transition is indirect $n = 1/2$) [59, 60].

Prior studies evaluating hematite (α-Fe$_2$O$_3$) band gap observed inconsistent results on whether it has direct or indirect bandgap; some has reported that hematite is a direct bandgap material [50, 61], while others described it as an indirect bandgap material [62, 63]. Differently, other demonstrated that α-Fe$_2$O$_3$ possess the both types of band gaps direct and indirect [64, 65]. Consequently, we have considered studying both direct and indirect band gap transmissions. The estimation of bandgap using Tauc's plot exhibited a value of 3.53 eV for direct transmissions and 2.83 eV for indirect transmissions. These results are in line with those of previous studies [50, 59]

3.1 Fourier Transform Infrared (FTIR) Spectroscopy

FTIR analysis was mainly employed to identify the biomolecules that participated in iron oxide nanoparticles reduction and stabilization by comparing the spectrum of the crude plant extract with the spectrum of the biosynthesized nanoparticles.

The resultant FTIR spectrum (Fig. 6a) has revealed on multiple absorption peaks that related to the different functional groups of the biomolecules presented in the *M. oleifera* extract.

The O–H stretching vibrations was observed at the broad peak centered at 3368 cm^{-1} [66], the two close peaks appeared at 2913 cm^{-1} and 2842 cm^{-1} are assigned to the methyl group C–H asymmetric and symmetric stretching vibrations respectively [67], the C=O and C=C stretching vibrations are distinguished by the peaks located 1650 cm^{-1} and 1453 cm^{-1} respectively [68]. The presence of amines group was noted by the C–N stretching vibration band appears as narrow peak around 1540 cm^{-1} [68]. In addition, the peaks centered at 1230 cm^{-1} and 1055 cm^{-1} are assigned to C–O stretching C–OH bending vibrations respectively [69]. The peaks appeared in *M. oleifera* extract spectrum confirms that it contains different polyphenolic compounds
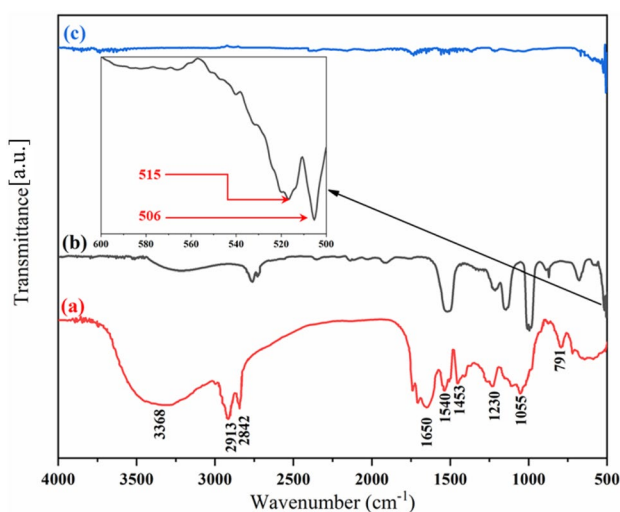

Fig. 6 FTIR Spectra of: **a** plant extract, **b** IONPs before annealing, and **c** IONPs after annealing

[67], that can effectively reduce and stabilize metals for nanoparticles biosynthesis [70].

Comparing the FTIR spectra of plant extract (Fig. 6a) and IONPs (Fig. 6b) show that there is a shift in the wavenumber of the absorption bands, which may indicate the interaction of biomolecules with iron ions [71]. Furthermore, the comparison exposed a distinguished decrease in intensity of the band centered at 3368 cm^{-1}, which indicates the vital role of the biomolecules attributed to this functional group in the reduction and stabilization of IONPs [57]. The wavenumber range from 500 to 600 cm^{-1} has been zoomed to display the inorganic peaks, the peaks shown at 506 cm^{-1} and 515 cm^{-1} are attributed to the Fe–O stretching vibrations [72, 73]. The same peaks were also seen in the spectrum of IONPs annealed (Fig. 6c), and all the executed runs.

3.2 X-Ray Diffraction (XRD)

Figure 7 shows all the XRD patterns of the different runs executed according to the experimental design order Table 3. Common peaks were observed in all the XRD patterns of the different runs placed at 2-theta (2θ) positions of 24.15°, 33.13°, 35.64°, 40.65°, 49.48°, 54.09°, 57.43°, 62.53°, and 64.14° assigned respectively to the crystal system of (012), (104), (110), (113), (024), (116), (122), (214) and (300) [74]. According to JCPDS card no. [33-066-4] these peaks are allocated to iron oxide of the type Hematite α-Fe$_2$O$_3$ of having its characteristic rhombohedral geometry and space group: R-3c (a = b = 5.04 Å, and c = 13.75 Å) [75].

As can be seen from Fig. 7 the peaks of XRD patterns vary in terms of intensity and width due to the different biosynthesis conditions. According to Scherrer's formula

(Eq. 2), these variations in peaks intensity and width indorse that these patterns correspond to samples of different crystallite sizes since the CR size is estimated from FWHM and peaks positions. The IONPs of the executed runs were of diverse sizes at the nanoscale range of 29.26–64.55 nm.
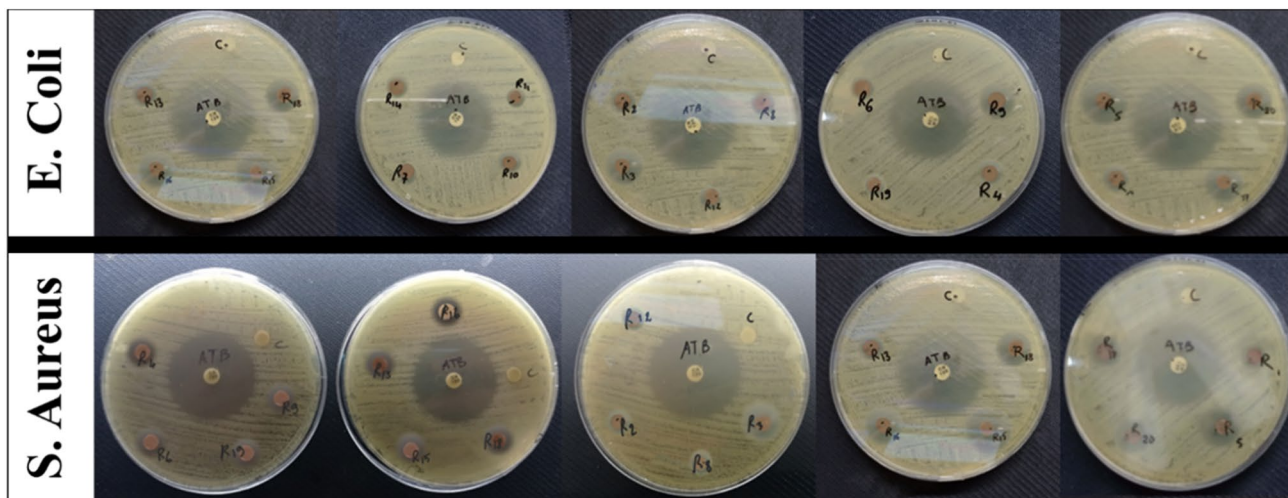
3.3 Antibacterial Activity

Figure 8 shows the antibacterial activity for the different runs of IONPs against both gram-positive and gram-negative bacteria. The results indicate that the biosynthesized nanoparticles and antibiotic (ATB) inhibited the growth of both gram-positive and gram-negative microorganisms. The antibiotic (ATB) discs exhibited an inhibition zone of 36.3 ± 1.98 mm and 32.7 ± 2.31 mm against *E. coli* and *S. aureus* respectively. Meanwhile no inhibition zone formed around the control discs (C) Table 4. On the other hand, the discs attributed to the designed runs of IONPs exhibited different sizes inhibition zones. The performed runs besides their inhibition zones are listed in Table 3.

3.4 Fitting of model

Tables 5 and 6 represent the ANOVA tables for IONPs antibacterial activity against both *E. coli* and *S. aureus* respectively. The analysis of variance tables indicates that both models are significant with P values less than 0.0001 and Fisher's F-values of 83.63 and 100.61 for *E. coli* and *S. aureus* inhibition zones respectively [76]. The studied terms effect on the antibacterial activity of IONPs can be obtained from the relation between the Fisher's F-value, p-value and term effect. The relation between F-value and
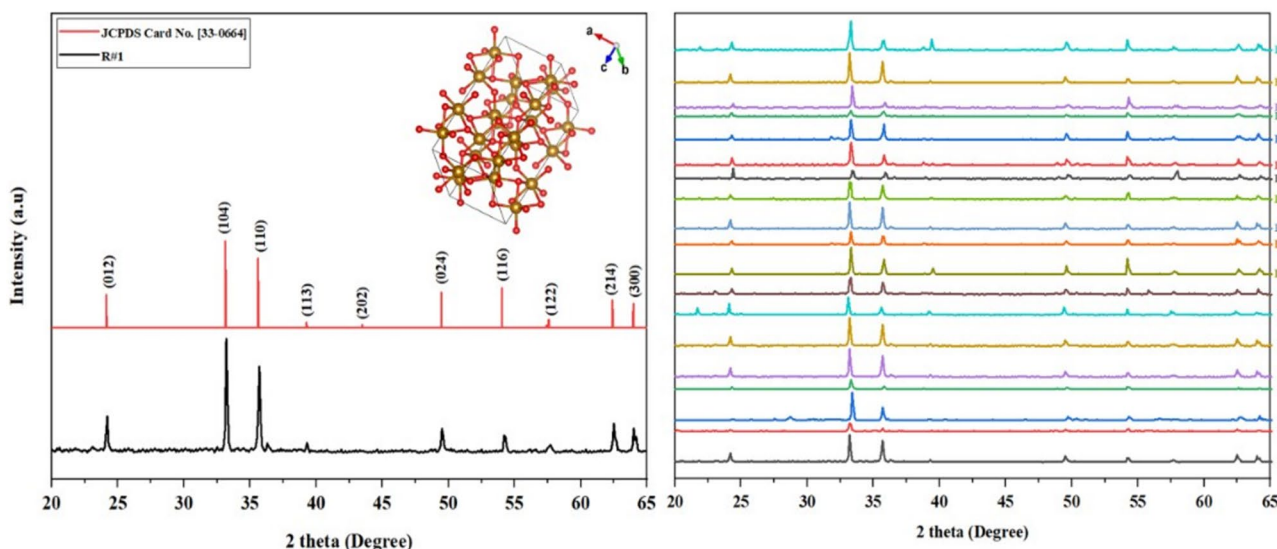
Fig. 7 X ray diffraction of Run 01 besides JCDPS refference card pattern [on the left] and the patterns of all the performed experiments [on the right]

Fig. 8 The antibacterial activity for the different runs of IONPs against *E. coli* and *S. aureus*

Table 4 Inhibition zones of ATB and control discs

Sample	Escherichia coli	Staphylococcus aureus
Control	0 mm	0 mm
Gentamicin (120 µg)	36.3 ± 1.98 mm	32.7 ± 2.31 mm

Table 5 ANOVA Table of IONPs antibacterial activity against *E. coli*

Source	Sum of squares	df	Mean square	F-value	p-value
Model	225.58	9	25.06	83.63	< 0.0001[a]
A-Pre-Con	85.14	1	85.14	284.08	< 0.0001
B-RC temp	4.68	1	4.68	15.60	0.0027
C-ANL temp	71.59	1	71.59	238.86	< 0.0001
AB	2.10	1	2.10	7.01	0.0244
AC	0.3612	1	0.3612	1.21	0.2980
BC	0.3612	1	0.3612	1.21	0.2980
A^2	25.13	1	25.13	83.84	< 0.0001
B^2	26.49	1	26.49	88.39	< 0.0001
C^2	21.88	1	21.88	72.99	< 0.0001
Residual	3.00	10	0.2997		
Lack of fit	1.58	5	0.3168	1.12	0.4518[b]
Pure error	1.41	5	0.2827		
Cor total	228.58	19			

Table 6 ANOVA Table of IONPs antibacterial activity against *S. aureus*

Source	Sum of squares	df	Mean square	F-value	p-value
Model	180.89	9	20.1	100.61	< 0.0001[a]
A-Pre-Con	65.72	1	65.72	328.96	< 0.0001
B-RC Temp	7.39	1	7.39	36.99	0.0001
C-ANL Temp	69.05	1	69.05	345.64	< 0.0001
AB	6.48	1	6.48	32.44	0.0002
AC	0.5	1	0.5	2.5	0.1447
BC	0.605	1	0.605	3.03	0.1124
A^2	13.63	1	13.63	68.23	< 0.0001
B^2	17.32	1	17.32	86.69	< 0.0001
C^2	5.84	1	5.84	29.24	0.0003
Residual	2	10	0.1998		
Lack of fit	1.34	5	0.2689	2.06	0.2236[b]
Pure error	0.6533	5	0.1307		
Cor total	182.89	19			

[a]Significant

[b]Not significant

p-value is inversely proportional, the higher the F-value the lower the p-value and the more significancy effect of term on the response, and verse versa [77]. In this case, for both *E. coli* and *S. aureus* responses, all the studied terms influence is significant except the interactive effects of BC and AC for both responses. The F-value also can be exploited to sort the effect significancy of the model terms, which was as follows: $A > C > B^2 > A^2 > C^2 > B > AB > AC > BC$. Demonstrating that the Pre-Con term (A) have the most significant effect on both model responses followed by ANL Temp [78].

Table 7 shows the different R square values for both responses. As can be seen the predicted R^2 value for both responses are very close to their adjusted R^2, and their coefficient of determination R^2. All the prementioned values are very close are unity 1 which approves the adequacy of the generated models [79]

Table 7 The different R square values for *E. coli* and *S. aureus* responses

Response	R^2	Adjusted R^2	Predicted R^2	Adeq precision
E. coli	0.9869	0.9751	0.9384	27.7517
S. Aureus	0.9891	0.9792	0.9389	32.7655

The analysis has revealed on a quadratic polynomial models' equation that link the responses with the studied factors are expressed by in terms of coded factors.

Exploiting RSM two mathematical quadratic models that links the responses with their independent variables were generated. The equations for both responses are expressed with coded factors in (Eqs. 8, 9).
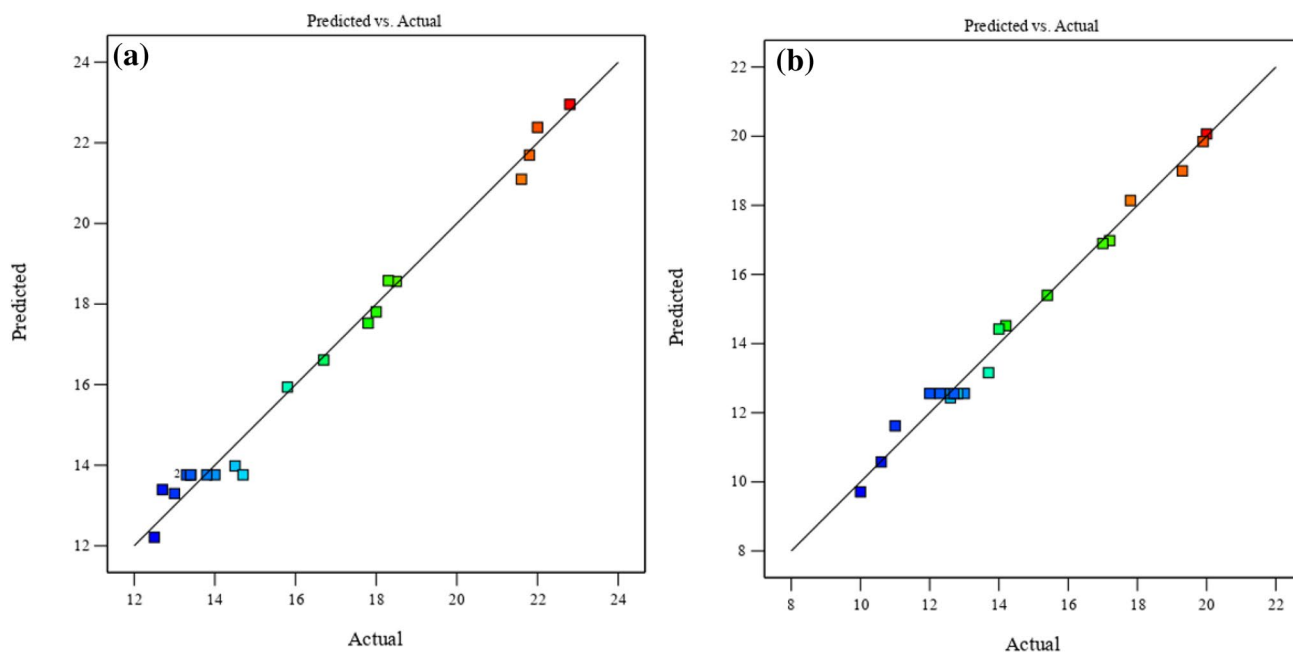
E. coli inhibition zone

$$Y_{E.\,coli} = 12.56 - 2.19A - 0.7356B - 2.25C - 0.9AB + 0.25AC + 0.275BC + 0.9725A^2 + 1.1B^2 + 0.6366C^2 \tag{8}$$
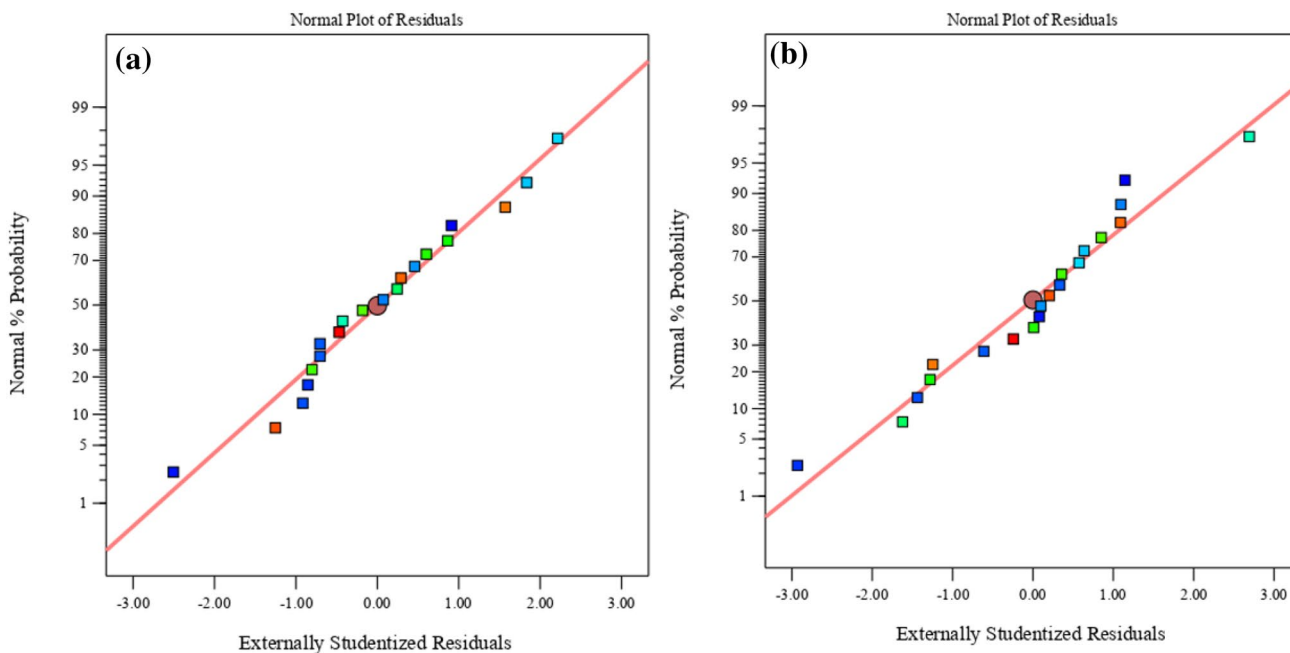
S. aureus inhibition zone

$$Y_{S.Aureus} = 12.56 - 2.19A - 0.7356B - 2.25C - 0.9AB + 0.25AC + 0.275BC + 0.9725A^2 + 1.1B^2 + 0.6366C^2 \tag{9}$$

These equations (Eqs. 8, 9) can be used to estimate the antibacterial activity of IONPs against *E. coli* and *S. aureus* for any value of the synthesis process variables. Which to obtain an enhanced antibacterial activity for our both responses. The equation describes the precisely the effect of each factor in two aspects, the term sign (positive or negative) represent the nature of its effect on the response, Meanwhile the term coefficient represents its effect intensity on the response [80]. According to (Eqs. 8 and 9) AB, AC, BC, A^2, B^2, C^2, has a positive effect on the response (*E. coli* and *S. aureus* inhibition zones), while the linear terms such A, B, and C have positive effects.

The predicted versus the actual values plots for E. coli response (Fig. 9a) and S. Aureus response (Fig. 9b). Shows

Fig. 9 The predicted values versus the observed values of **a** *E. coli* and **b** *S. aureus* inhibition zones

Fig. 10 The normal %probability residuals and studentized residuals for **a** *E. coli* and **b** *S. aureus* inhibition zones

that both responses predicted values are in close agreement with the experimental values, indicating the models proficiency in the prediction [81].

3.5 Internal vs. Normal

This normal probability plot shown in Fig. 10 is very helpful it shows whether the data are normally distributed or not. If the data forms a linear pattern means that the data is normally distributed and verse versa. In this case, the
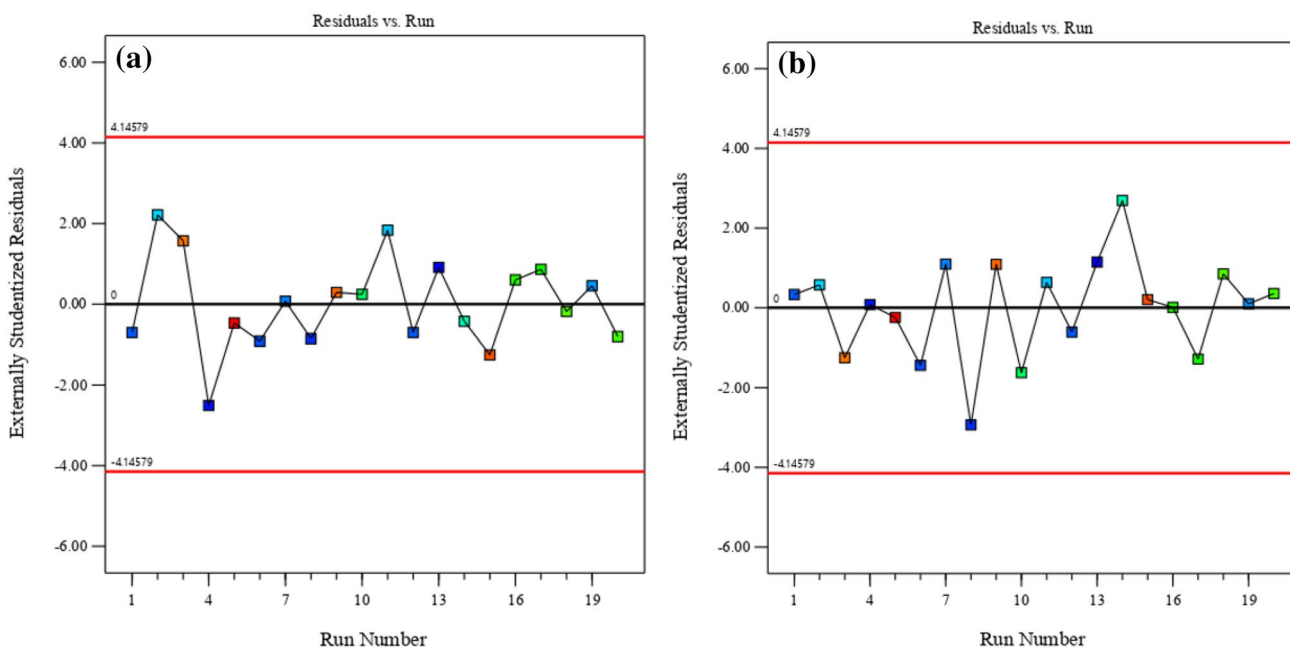
Fig. 11 The externally studentized residuals and run number for **a** *E. coli* and **b** *S. aureus* inhibition zones

data is distributed approximately in a straight line, which indicates that data is normally distributed [82, 83].

3.6 Residual's Analysis

The plot of residuals versus the run number is shown in Fig. 11, this plot is also reffered to as outlier t. The red lines on top and bellow the plot are identical to 95% confidence for the control range. The residual points should be inside the controle range (between the two red lines) in this case, all the points are inside the acceptable range. Furthermore, the plot shows a randomly scattred points without an obvious trend or shape being formed by the data points indicating the normal disterbution of residuals excluding any serial correlation.
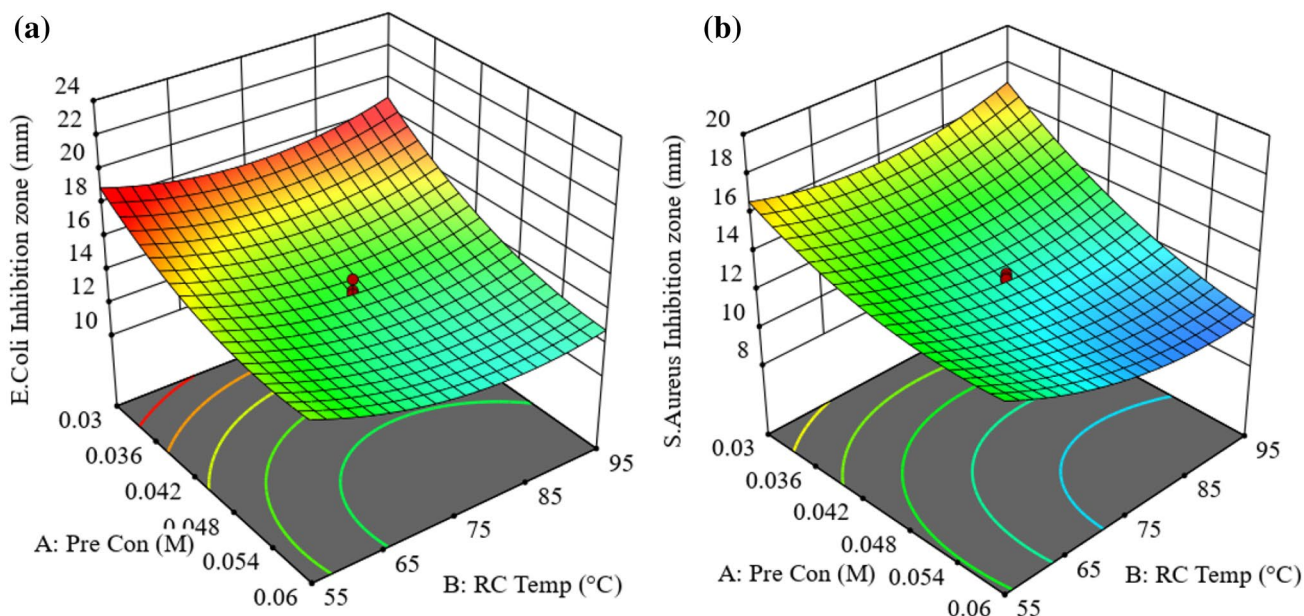

Fig. 12 3D surface plots of interaction between the Pre-Con and RC Temp on the **a** *E. coli* and **b** *S. aureus* inhibition zones
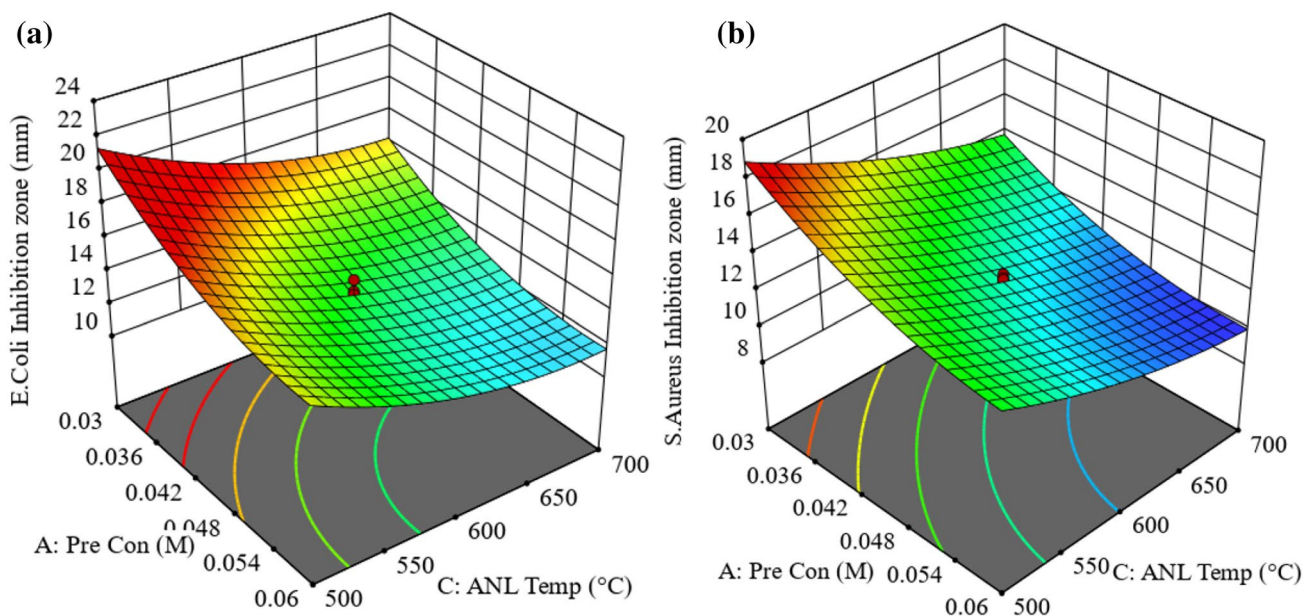

Fig. 13 3D surface plots of interaction between volume ANL Temp and Pre-Con on **a** *E. coli* and **b** *S. aureus* inhibition zones

3.7 Response Surface Plots

The interactive effect of the biosynthesis variables and their influence on gram-positive and gram-negative bacteria (*Staphylococcus aureus* and *Escherichia coli* respectively), is represented with three-dimensional (3D) contour plots of the response surface for every interaction of two factors were plotted while keeping the remaining process variable at its central (0) level.

The 3D surface plots in (Fig. 12) represent the combined effect of the Pre-Con and the RC Temp on the (a) *E. coli* and (b) *Aureus* inhibition zones. It is noted that a higher antibacterial activity of IONPs at lower levels of Pre-Con. Meanwhile, increasing both of Pre-Con and RC Temp have decreased the antibacterial activity of IONPs significantly.

Figure 13 shows the response surface with respect to Pre-Con and ANL Temp. The contour plot indicates that
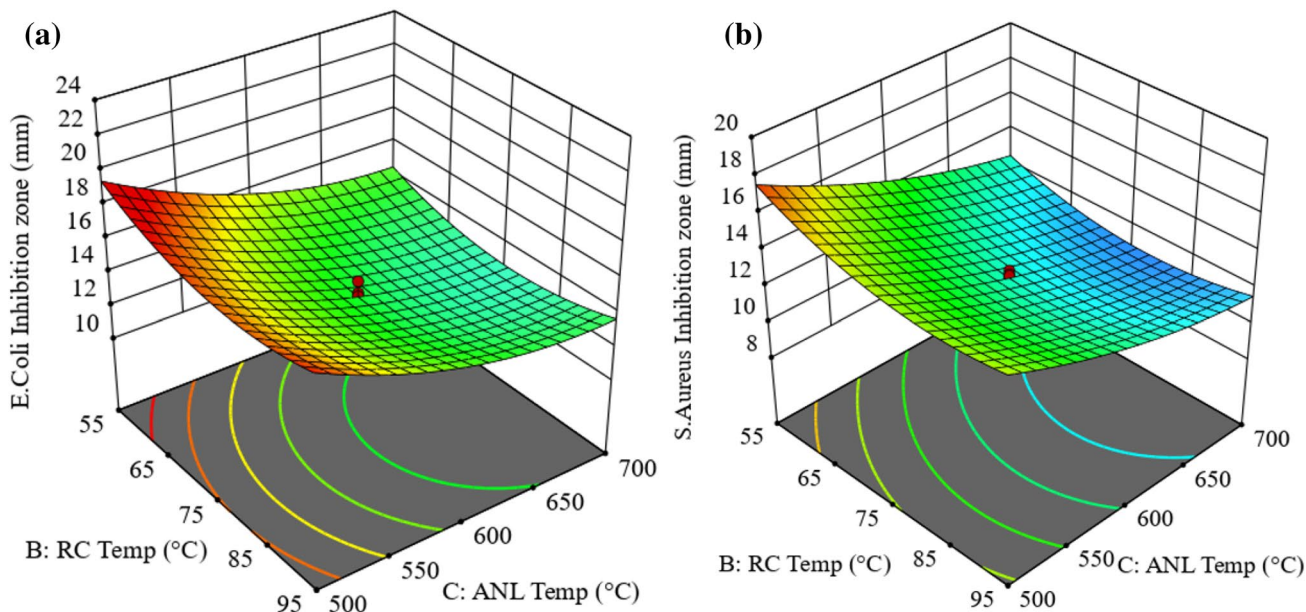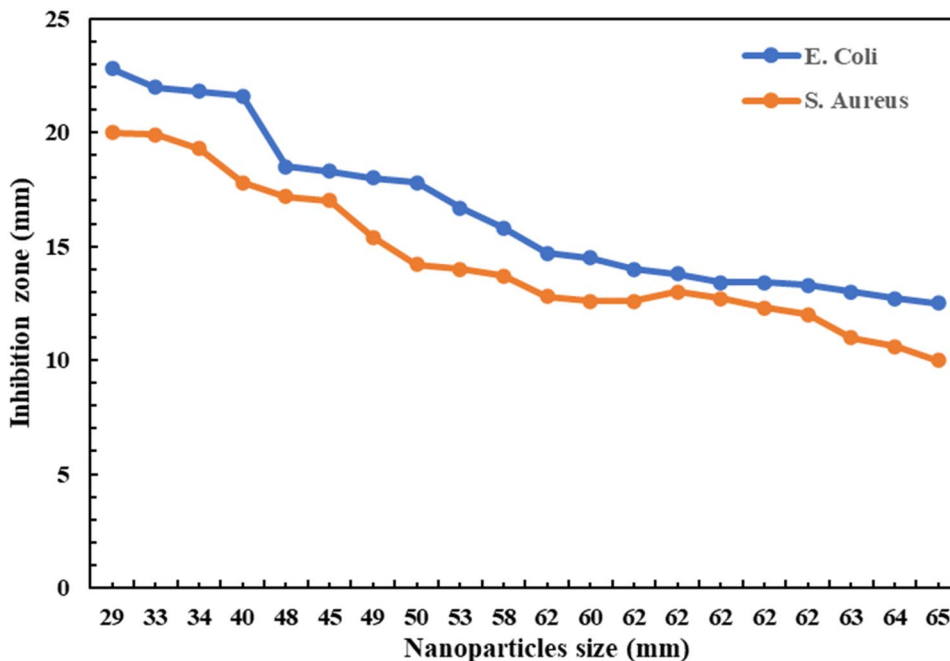

Fig. 14 3D surface plots of interaction between ANL Temp and RC Temp on **a** *E. coli* and **b** *S. aureus* inhibition zones

Fig. 15 The effect of IONPs size on the antibacterial activity against *E. coli* and *S. aureus*

IONPs antibacterial activity increases significantly by decreasing both Pre-Con and ANL Temp.

Figure 14 Shows that increasing ANL Temp have decreased IONPs antibacterial activity. Meanwhile, increasing the RC Temp from 55 to 75 °C have decreased the inhibition zones for both gram-positive gram-negative bacteria. However, further increase in RC Temp (more than 75 °C) have increased the antibacterial activity slightly.

To investigate the effect of IONPs crystallite size on their antibacterial activity against gram-positive and gram-negative bacteria, the crystallite size of each run was plotted against their inhibition zone Fig. 15, higher antibacterial activity was obtained at lower crystallite sizes. In other words, decreasing the crystallite size increases the antibacterial activity. This result is in accord with recent studies indicating that the smaller the nanoparticles size the higher antibacterial activity; the smaller sizes NP penetrates in to the cell easier compared the bigger counterparts, which causing more damage to the bacteria [70, 84–86]. Comparing the inhibition zones for each sample against gram-positive and gram-negative bacteria shows that gram-negative bacteria have more significant inhabitation zones. Pervious study have demonstrated that the variance in antibacterial activity is due to the differences in each bacteria type's construction and composition of cell membranes [87]. Gram-negative bacteria have thinner peptidoglycan cell membranes compared to Gram-positive bacteria. Therefore, IONPs penetrates it easier, causing a higher antibacterial activity [88].

The results observed in Figs. 12 and 14 demonstrates a trend behavior for RC Temp effect on the antibacterial activity; increasing the RC Temp decreases the antibacterial activity meanwhile at high temperatures (more than 80 °C in this work) causes a slight increase in IONPs antibacterial activity. This finding broadly supports the work of previous studies linking RC Temp with nanoparticles crystallite size [31]. Which explained this increase of crystallite size with the fact that increasing RC Temp increases the nucleation rate, resulting in more precursor monomers to be consumed and become crystal nucleus. At this point, if the precursor concentration is sufficient, the precursors would grow faster on the nucleus due to the increased growth rate at high temperatures. In contrast, if there is unsatisfaction in precursor concentration, the growth would be limited due to the lack of precursor monomers. Consequently, the crystallite size of the NPs decreases [31]. Decreasing IONPs crystallite size facilitates their penetration throw the bacteria cell causing more damage to the bacteria consequently more antibacterial activity is obtained at lower levels of RC Temp in other words, the decreased RC Temp levels decreases the size of IONPs which enhance their antibacterial activity [70, 84–86].

The inverse relation between the antibacterial activity and Perc Con shown in Figs. 12 and 13 can be also explained by the direct proportional correlation between crystallite size and Pre-Con [28, 50]. The increase of the precursor concentration with sufficient surfactants, increases the concentration of monomers by increasing the number of monomers (growth species) at the same volume. Consequently, the diffusion distance between monomers decreases, leading to higher mass transfer and higher growth. As a result, the crystallite size increases which makes it more difficult for the nanoparticles to penetrate the bacteria cell causing a decrease on the IONPs antibacterial activity [28, 70, 84–86]

According to Figs. 13 and 14 results, the increase in crystallite size is inversely proportional to ANL Temp. This observation may support the hypothesis that increasing annealing temperature increases the amount of thermal energy given to the nanoparticles, leading them to earn a sufficient energy for diffusive motion in what is known by the Oswald ripening process [89]. which is a diffusion process where bigger particles are formed at the expense of small particles [90, 91]. As a result, the crystallite size increases which restricts the nanoparticles to penetration the bacteria cell causing a decrease on the IONPs antibacterial activity [70, 84–86].

3.8 Optimization Using the Desirability Functions

The antibacterial activity of IONPs optimization was performed using the desirability functions. *Design expert 13* software allows to set optimization goals to minimize, maximize, obtain a targeted value or obtain a solution in specific range of the response. In this study, the optimization goal was set to maximize the antibacterial activity while setting all the factors ranges between their maximum (+1) and minimum (− 1) levels. Using the previous optimization criteria, a maximum desirability of 0.857 associated with maximum antibacterial activity represented with maximum inhibition zones for both E. coli and S. Aureus of 22.95 mm and 20 mm respectively. The maximum antibacterial activity was achieved by setting all the biosynthesis parameters at their inferior levels; i.e., Pre-Con = 0.03 M, RC Temp = 55 °C and ANL Temp 500 °C. The optimal condition and their related desirability are shown in Fig. 16 The experimental run executed at the suggested optimal conditions exhibited an antibacterial activity of 22.55 mm and 19.15 mm for both E. coli and S. Aureus respectively, which is in close arrangement with the predicted response, approving the model prediction adequacy in the studied range.
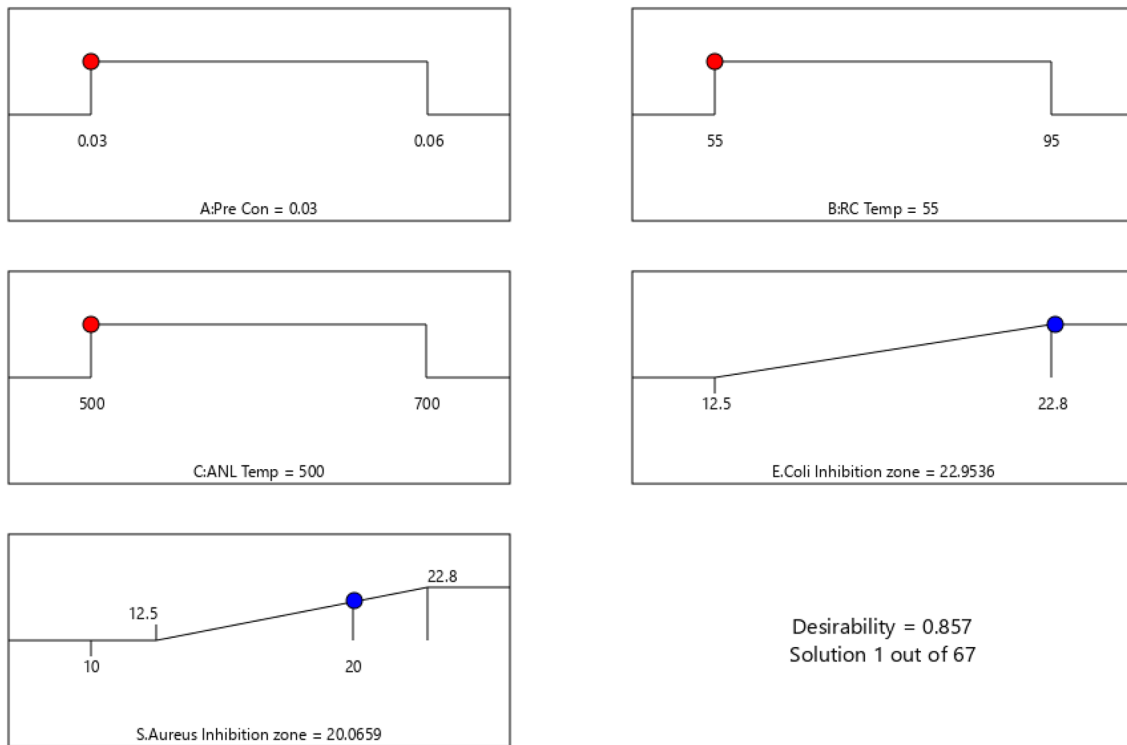
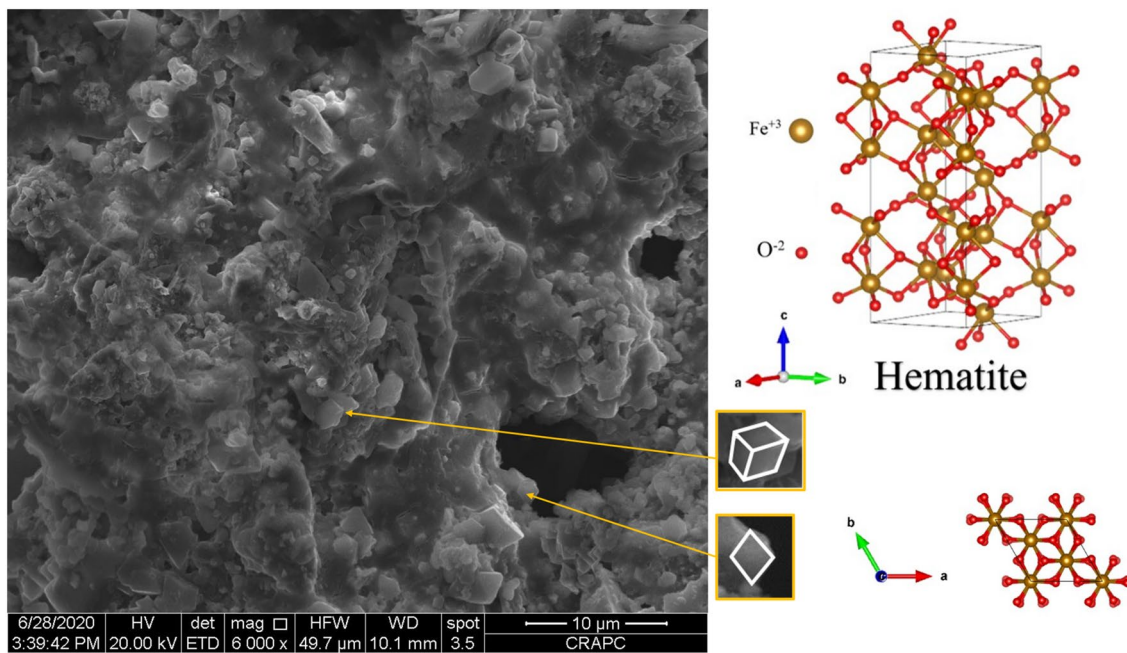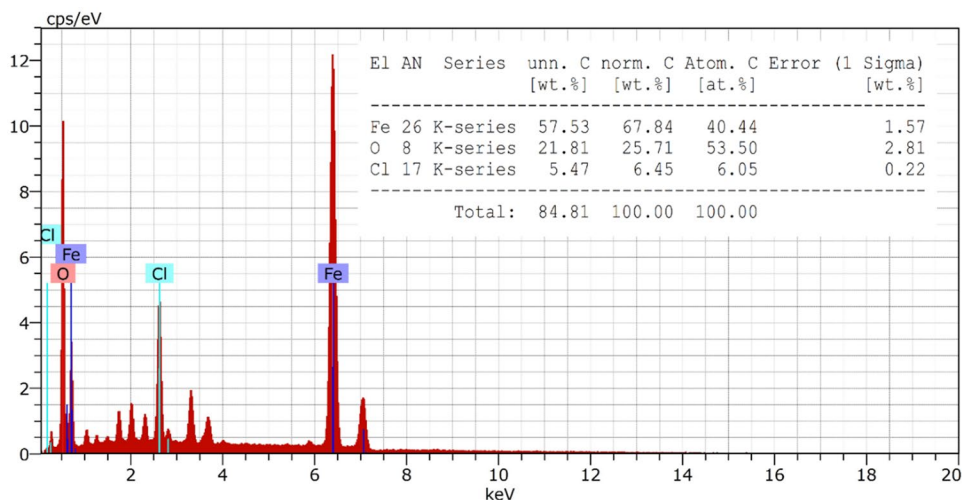**Fig. 16** Desirability ramp for optimization

Fig. 17 SEM image for the biosynthesized IONPs under the optimum antibacterial activity

Fig. 18 EDX spectrum of Iron oxide NPs at the optimal conditions

3.9 Scanning Electron Microscopy (SEM)

The SEM analysis exhibited an image shown in Fig. 17, between the diverse irregular shapes, it's possible to recognize a majority trend of distorted cubes (rhombohedral) structure placed as an aggregated form with a minority of dispersed separate particles. Which further support XRD findings, similar results were demonstrated in prior studies [50, 92].

3.10 The Energy Dispersive X-Ray Analysis (EDX)

EDX was employed to identify the elemental composition of biosynthesized iron oxide nanoparticles at the optimal conditions (Fig. 18). The spectrum shown that the sample contains of both Iron (Fe) and Oxygen (O) with different quantities. The weight percentages of Iron and Oxygen were 67.84% and 25.71% respectively. The spectrum also shows the presence of unimportant fraction of Chlorine which may be due to the mineral cell used. Similar results were stated in former works [93, 94].

4 Conclusion

In this paper, deign of experiments (DoE) was exploited to investigate the combined and individual effect of diverse biosynthesis parameters on the antibacterial activity of IONPs against-gram positive and gram-negative bacteria. The characterization results indicated the successful synthesis of IONPs using *M. oleifera* extract and their antibacterial activity was tested.

The findings have proven the validity of the generated quadratic model and its adequacy in predicting and fitting the experimental data, that makes it appropriate to study and optimize the antibacterial activity of IONPs. The analysis of variance indicated that the antibacterial activity of IONPs can be significantly affected by precursor concentration, reaction temperature and annealing temperature and their interactive effect. However, the precursor concentration (A) and the interaction between precursor concentration and reaction temperature (AB) has more significant effect on the antibacterial activity of IONPs against both gram positive and gram negative comparing to the other factors.

Optimal antibacterial activity was achieved exploiting the numerical optimization and the desirability function, setting the optimization goal to maximize the antibacterial activity of both gram-positive and gram-negative bacteria. As a result, the maximum antibacterial activity related to inhibition zones of 22.95 mm for *E. coli* and 20 mm for *S. aureus* respectively was achieved by setting all the biosynthesis parameters at their inferior levels, i.e., precursor concentration = 0.03 M, reaction temperature = 55 °C and annealing temperature 500 °C. The confirmatory run executed at the suggested optimal conditions exhibited a very close result to the expected value. The current study has proven the efficiency of response surface methodology as an efficient technique to study and optimize the antibacterial activity of nanomaterials.

Further future investigations may consider preforming more comprehensive study by involving more bacteria types and more parameters added to the ones studied in this work, which may permit generating more efficient and comprehensive mathematical model.

Declarations

Conflict of interest The authors declare that they have no conflict of interest.

References

1. M.-C. Daniel, D. Astruc, Gold nanoparticles: assembly, supramolecular chemistry, quantum-size-related properties, and applications toward biology, catalysis, and nanotechnology. Chem. Rev. **104**, 293–346 (2004). https://doi.org/10.1021/cr030698
2. W. Wu, C.J. Changzhong Jiang, V.A.L. Roy, Recent progress in magnetic iron oxide–semiconductor composite nanomaterials as promising photocatalysts. Nanoscale **7**, 38–58 (2015). https://doi.org/10.1039/C4NR04244A
3. M. Rui, C. Ma, Y. Hao, J. Guo, Y. Rui, X. Tang, Q. Zhao, X. Fan, Z. Zhang, T. Hou, S. Zhu, Iron oxide nanoparticles as a potential iron fertilizer for peanut (*Arachis hypogaea*). Front. Plant Sci. **7**, 815–825 (2016). https://doi.org/10.3389/fpls.2016.00815
4. P. Xu, G.M. Zeng, D.L. Huang, C.L. Feng, S. Hu, M.H. Zhao, C. Lai, Z. Wei, C. Huang, G.X. Xie, Z.F. Liu, Use of iron oxide nanomaterials in wastewater treatment: a review. Sci. Total Environ. **424**, 1–10 (2012). https://doi.org/10.1016/j.scitotenv.2012.02.023
5. A.A. Hernández-Hernández, G. Aguirre-Álvarez, R. Cariño-Cortés, L.H. Mendoza-Huizar, R. Jiménez-Alvarado, Iron oxide nanoparticles: synthesis, functionalization, and applications in diagnosis and treatment of cancer. Chem. Pap. **74**, 3809–3824 (2020). https://doi.org/10.1007/s11696-020-01229-8
6. C.F. Chee, B.F. Leo, C.W. Lai, Superparamagnetic iron oxide nanoparticles for drug delivery, in *Applications of Nanocomposite Materials in Drug Delivery*. ed. by I. Inamuddin, A.M. Asiri, A. Mohammad (Elsevier, Amsterdam, 2018), pp. 861–903
7. A. Joy, G. Unnikrishnan, M. Megha, M. Haris, J. Thomas, E. Kolanthai, S. Muthuswamy, Polycaprolactone/graphene oxide-silver nanocomposite: a multifunctional agent for biomedical applications. J. Inorg. Organomet. Polym. Mater. **32**, 912–930 (2022). https://doi.org/10.1007/s10904-021-02180-1
8. T. Li, P. Huang, X. Li, R. Wang, Z. Lu, P. Song, Y. He, Synthesis of polymer nanospheres conjugated Ce (IV) complexes for constructing double antibacterial centers. J. Inorg. Organomet. Polym. Mater. **32**, 883–894 (2022). https://doi.org/10.1007/s10904-021-02165-0
9. M. Moosavifar, G. Zarrini, E. Mashmool-barjasteh, Design of Zn1−xCuxO nanocomposite Ag-doped as an efficient antimicrobial agent. J. Inorg. Organomet. Polym. Mater. **32**, 781–790 (2022). https://doi.org/10.1007/s10904-021-02131-w
10. F.Z. Souissi, M. Hajji, H. Ettoumi, M. Barre, J. Benkhalifa, T. Guerfel, Synthesis, thermal properties and electrical conductivity of Na-sialate geopolymer. J. Inorg. Organomet. Polym. Mater. (2022). https://doi.org/10.1007/s10904-022-02337-6
11. D.E. Bloom, D. Cadarette, Infectious disease threats in the twenty-first century: strengthening the global response. Front. Immunol. **10**, 549 (2019). https://doi.org/10.3389/fimmu.2019.00549
12. P.V. Baptista, M.P. McCusker, A. Carvalho, D.A. Ferreira, N.M. Mohan, M. Martins, A.R. Fernandes, Nano-strategies to fight multidrug resistant bacteria-"A Battle of the Titans". Front. Microbiol. **9**, 1441 (2018). https://doi.org/10.3389/fmicb.2018.01441
13. L. Lin, S.F. Wang, T.Y. Yang, W.C. Hung, M.Y. Chan, S.P. Tseng, Antimicrobial resistance and genetic diversity in ceftazidime non-susceptible bacterial pathogens from ready-to-eat street foods in three Taiwanese cities. Sci. Rep. **7**, 1–9 (2017). https://doi.org/10.1038/s41598-017-15627-8
14. N. Jackson, L. Czaplewski, L.J.V. Piddock, Discovery and development of new antibacterial drugs: learning from experience? J. Antimicrob. Chemother. **73**, 1452–1459 (2018). https://doi.org/10.1093/jac/dky019
15. S. Das, S. Diyali, G. Vinothini, B. Perumalsamy, G. Balakrishnan, T. Ramasamy, D. Dharumadurai, B. Biswas, Synthesis, morphological analysis, antibacterial activity of iron oxide nanoparticles and the cytotoxic effect on lung cancer cell line. Heliyon **6**, e04953 (2020). https://doi.org/10.1016/j.heliyon.2020.e04953
16. G. Saxena, R. Chandra, R.N. Bharagava, Environmental pollution, toxicity profile and treatment approaches for tannery wastewater and its chemical pollutants. Rev. Environ. Contam. Toxicol. **240**, 31–69 (2017). https://doi.org/10.1007/398_2015_5009
17. S. Soren, S. Kumar, S. Mishra, P.K. Jena, S.K. Verma, P. Parhi, Evaluation of antibacterial and antioxidant potential of the zinc oxide nanoparticles synthesized by aqueous and polyol method. Microb. Pathog. **119**, 145–151 (2018). https://doi.org/10.1016/j.micpath.2018.03.048
18. S.F. Mossallam, E.I. Amer, R.G. Diab, Potentiated anti-microsporidial activity of *Lactobacillus acidophilus* CH1 bacteriocin using gold nanoparticles. Exp. Parasitol. **144**, 14–21 (2014). https://doi.org/10.1016/j.exppara.2014.06.002
19. H. Mohd Yusof, R. Mohamad, U.H. Zaidan, N.A. AbdulRahman, Microbial synthesis of zinc oxide nanoparticles and their potential application as an antimicrobial agent and a feed supplement in animal industry: a review. J. Anim. Sci. Biotechnol. **10**, 57 (2019). https://doi.org/10.1186/s40104-019-0368-z
20. T.M. Laid, K. Abdelhamid, L.S. Eddine, B. Abderrhmane, Optimizing the biosynthesis parameters of iron oxide nanoparticles using central composite design. J. Mol. Struct. (2020). https://doi.org/10.1016/j.molstruc.2020.129497
21. L. Chen, J. Xie, H. Wu, J. Li, Z. Wang, L. Song, F. Zang, M. Ma, N. Gu, Y. Zhang, Precise study on size-dependent properties of magnetic iron oxide nanoparticles for in vivo magnetic resonance imaging. J. Nanomater. **2018**, 1–9 (2018). https://doi.org/10.1155/2018/3743164
22. V. Patsula, M. Moskvin, S. Dutz, D. Horák, Size-dependent magnetic properties of iron oxide nanoparticles. J. Phys. Chem. Solids. **88**, 24–30 (2016). https://doi.org/10.1016/j.jpcs.2015.09.008
23. H. Parmar, I.S. Smolkova, N.E. Kazantseva, V. Babayan, P. Smolka, R. Moučka, J. Vilcakova, P. Saha, Size dependent heating efficiency of iron oxide single domain nanoparticles. Proc. Eng. **102**, 527–533 (2015). https://doi.org/10.1016/j.proeng.2015.01.205
24. M. Arakha, S. Pal, D. Samantarrai, T.K. Panigrahi, B.C. Mallick, K. Pramanik, B. Mallick, S. Jha, Antimicrobial activity of iron oxide nanoparticle upon modulation of nanoparticle-bacteria interface. Sci. Rep. **5**, 14813 (2015). https://doi.org/10.1038/srep14813
25. J.P. Yadav, S. Kumar, Characterization and antibacterial activity of synthesized silver and iron nanoparticles using aloe vera. J. Nanomed. Nanotechnol. **7**, 2 (2016). https://doi.org/10.4172/2157-7439.1000384
26. H. Padalia, S. Baluja, S. Chanda, Effect of pH on size and antibacterial activity of *Salvadora oleoides* leaf extract-mediated synthesis of zinc oxide nanoparticles. Bionanoscience **7**, 40–49 (2017). https://doi.org/10.1007/s12668-016-0387-6
27. W. Xie, Z. Guo, F. Gao, Q. Gao, D. Wang, B. Liaw, Q. Cai, X. Sun, X. Wang, L. Zhao, Shape-, size- and structure-controlled synthesis and biocompatibility of iron oxide nanoparticles for magnetic theranostics. Theranostics **8**, 3284–3307 (2018). https://doi.org/10.7150/thno.25220
28. H. Sharifi Dehsari, A. Halda Ribeiro, B. Ersöz, W. Tremel, G. Jakob, K. Asadi, Effect of precursor concentration on size

evolution of iron oxide nanoparticles. CrystEngComm **19**, 6694–6702 (2017). https://doi.org/10.1039/c7ce01406f

29. Â.L. Andrade, D.M. Souza, M.C. Pereira, J.D. Fabris, R.Z. Domingues, pH effect on the synthesis of magnetite nanoparticles by the chemical reduction-precipitation method. Quim. Nova. **33**, 524–527 (2010). https://doi.org/10.1590/S0100-40422010000300006

30. E. Ranjith Kumar, R. Jayaprakash, T. ArunKumar, S. Kumar, Effect of reaction time on particle size and dielectric properties of manganese substituted CoFe2O4 nanoparticles. J. Phys. Chem. Solids. **74**, 110–114 (2013). https://doi.org/10.1016/j.jpcs.2012.08.008

31. H. Liu, H. Zhang, J. Wang, J. Wei, Effect of temperature on the size of biosynthesized silver nanoparticle: deep insight into microscopic kinetics analysis. Arab. J. Chem. **13**, 1011–1019 (2020). https://doi.org/10.1016/j.arabjc.2017.09.004

32. N. Chomchoey, D. Bhongsuwan, T. Bhongsuwan, Effect of calcination temperature on the magnetic characteristics of synthetic iron oxide magnetic nanoparticles for arsenic adsorption. Chiang Mai J. Sci. **45**, 528–539 (2018)

33. A. Dharr, A. Arjun, T. Raguram, K.S. Rajni, Influence of pH on the structural, spectral, optical, morphological and photocatalytic properties of ZrO2 nanoparticles synthesized by sol–gel technique. J. Mater. Sci. Mater. Electron. **31**, 15718–15730 (2020)

34. C. Yuangyai, H.B. Nembhard, Design of experiments: a key to innovation in nanotechnology, in *Emerging Nanotechnologies for Manufacturing*. ed. by W. Ahmed, M. Jackson (Boston, Elsevier, 2010), pp. 207–234

35. S. Saif, A. Tahir, Y. Chen, Green synthesis of iron nanoparticles and their environmental applications and implications. Nanomaterials (2016). https://doi.org/10.3390/nano6110209

36. K. Hinkelmann, *Design and Analysis of Experiments* (Wiley, Hoboken, 2012)

37. A. Tedjani, A. Benallal, Correction to: A novel cost-effective sparsity-aware algorithm with Kalman-based gain for the identification of long acoustic impulse responses (Signal, Image and Video Processing, (2020), 14, 8, (1679–1687), 10.1007/s11760-020-01715-2). Signal Image Video Process. **15**, 439 (2021). https://doi.org/10.1007/s11760-020-01739-8

38. A.A. Mariod, M.E. SaeedMirghani, I. Hussein, Chapter 35—*Moringa oleifera* seed oil, in *Unconventional Oilseeds and Oil Sources*. ed. by A.A. Mariod, M.E. SaeedMirghani, O.S. Hussein (Academic Press, Cmbridge, 2017), pp. 233–241

39. H.S.U. Rebecca, M. Sharon, A. Arbainsyah, D. Lucienne, *Moringa oleifera*: medicinal and socio-economic uses. Int. Course Econ. Bot. **2006**, 2–6 (2006)

40. S.M. Abdulkarim, K. Long, O.M. Lai, S.K.S. Muhammad, H.M. Ghazali, Some physico-chemical properties of *Moringa oleifera* seed oil extracted using solvent and aqueous enzymatic methods. Food Chem. **93**, 253–263 (2005). https://doi.org/10.1016/j.foodchem.2004.09.023

41. S.E. Laouini, A. Bouafia, A.V. Soldatov, H. Algarni, M.L. Tedjani, G.A.M. Ali, A. Barhoum, Green synthesized of Ag/Ag2O nanoparticles using aqueous leaves extracts of *Phoenix dactylifera* L. and their azo dye photodegradation. Membranes (2021). https://doi.org/10.3390/membranes11070468

42. Y. Belaiche, A. Khelef, S.E. Laouini, A. Bouafia, M.L. Tedjani, A. Barhoum, Green synthesis and characterization of silver/silver oxide nanoparticles using aqueous leaves extract of artemisia herba-alba as reducing and capping agents. Rev. Rom. Mater. **51**, 342–352 (2021)

43. F.T. Thema, P. Beukes, A. Gurib-Fakim, M. Maaza, Green synthesis of monteponite CdO nanoparticles by *Agathosma betulina* natural extract. J. Alloys Compd. **646**, 1043–1048 (2015). https://doi.org/10.1016/j.jallcom.2015.05.279

44. A.T. Khalil, M. Ovais, I. Ullah, M. Ali, Z.K. Shinwari, M. Maaza, Biosynthesis of iron oxide (Fe2O3) nanoparticles via aqueous extracts of *Sageretia thea* (Osbeck.) and their pharmacognostic properties. Green Chem. Lett. Rev. **10**, 186–201 (2017). https://doi.org/10.1080/17518253.2017.1339831

45. A. Bouafia, S.E. Laouini, M.L. Tedjani, G.A.M. Ali, A. Barhoum, Green biosynthesis and physicochemical characterization of Fe3O4 nanoparticles using *Punica granatum* L. fruit peel extract for optoelectronic applications. Text. Res. J. (2021). https://doi.org/10.1177/00405175211006671

46. A. Bouafia, S.E. Laouini, A. Khelef, M.L. Tedjani, F. Guemari, Effect of ferric chloride concentration on the type of magnetite (Fe3O4) nanoparticles biosynthesized by aqueous leaves extract of *Artemisia* and assessment of their antioxidant activities. J. Clust. Sci. (2020). https://doi.org/10.1007/s10876-020-01868-7

47. O. Louafi, A. Khelef, S. Zeroual, S.E. Laouini, M.L. Tedjani, Effect of nickel nitrate concentration on the size of nickel oxide nanoparticles bio-synthesized by artemisia herba-alba aqueous leaves extract and improving their antioxidant activities. J. Inorg. Organomet. Polym. Mater. (2021). https://doi.org/10.1007/s10904-021-02152-5

48. J.I. Langford, X-ray diffraction procedures for polycrystalline and amorphous materials by H. P. Klug and L. E. Alexander. J. Appl. Crystallogr. **8**, 573–574 (1975). https://doi.org/10.1107/S0021889875011399

49. H. Amiri, R. Nabizadeh, S. Silva Martinez, S. Jamaleddin Shahtaheri, K. Yaghmaeian, A. Badiei, S. Nazmara, K. Naddafi, Response surface methodology modeling to improve degradation of chlorpyrifos in agriculture runoff using TiO2 solar photocatalytic in a raceway pond reactor. Ecotoxicol. Environ. Saf. **147**, 919–925 (2018). https://doi.org/10.1016/j.ecoenv.2017.09.062

50. A. Bouafia, S.E. Laouini, Green synthesis of iron oxide nanoparticles by aqueous leaves extract of *Mentha pulegium* L.: effect of ferric chloride concentration on the type of product. Mater. Lett. **265**, 127364–127368 (2020). https://doi.org/10.1016/j.matlet.2020.127364

51. J.K. Patra, K.-H. Baek, Green nanobiotechnology: factors affecting synthesis and characterization techniques. J. Nanomater. **2014**, 1–12 (2014). https://doi.org/10.1155/2014/417305

52. J.A.A. Abdullah, L. Salah Eddine, B. Abderrhmane, M. Alonso-González, A. Guerrero, A. Romero, Green synthesis and characterization of iron oxide nanoparticles by pheonix dactylifera leaf extract and evaluation of their antioxidant activity. Sustain. Chem. Pharm. **17**, 100280–100287 (2020). https://doi.org/10.1016/j.scp.2020.100280

53. G.E.P. Box, J.S. Hunter, Multi-factor experimental designs for exploring response surfaces. Ann. Math. Stat. **28**, 195–241 (1957). https://doi.org/10.1214/aoms/1177707047

54. X. Zhang, J. Chen, M. Mao, H. Guo, Y. Dai, Extraction optimization of the polysaccharide from *Adenophorae* radix by central composite design. Int. J. Biol. Macromol. **67**, 318–322 (2014). https://doi.org/10.1016/j.ijbiomac.2014.03.039

55. P. Mondal, M.K. Purkait, Green synthesized iron nanoparticles supported on pH responsive polymeric membrane for nitrobenzene reduction and fluoride rejection study: optimization approach. J. Clean. Prod. **170**, 1111–1123 (2018). https://doi.org/10.1016/j.jclepro.2017.09.222

56. D. Badmapriya, I.V. Asharani, Dye degradation studies catalysed by green synthesized iron oxide nanoparticles. Int. J. ChemTech Res. **9**, 409–416 (2016)

57. S. Groiss, R. Selvaraj, T. Varadavenkatesan, R. Vinayagam, Structural characterization, antibacterial and catalytic effect of iron oxide nanoparticles synthesised using the leaf extract of *Cynometra ramiflora*. J. Mol. Struct. **1128**, 572–578 (2017). https://doi.org/10.1016/j.molstruc.2016.09.031

58. W.H. Strehlow, E.L. Cook, Compilation of energy band gaps in elemental and binary compound semiconductors and insulators. J. Phys. Chem. Ref. Data. **2**, 163–200 (1973). https://doi.org/10.1063/1.3253115

59. P. Mallick, B.N. Dash, X-ray diffraction and UV-visible characterizations of α-Fe2O3 nanoparticles annealed at different temperature. J. Nanosci. Nanotechnol. **3**, 130–134 (2013). https://doi.org/10.5923/j.nn.20130305.04

60. P. Jayaprakash, M.P. Mohamed, M.L. Caroline, Growth, spectral and optical characterization of a novel nonlinear optical organic material: d-Alanine dl-Mandelic acid single crystal. J. Mol. Struct. **1134**, 67–77 (2017). https://doi.org/10.1016/j.molstruc.2016.12.026

61. M. Gartner, M. Crisan, A. Jitianu, R. Scurtu, R. Gavrila, I. Oprea, M. Zaharescu, Spectroellipsometric characterization of multilayer sol-gel Fe2O3 films. J. Sol-Gel Sci. Technol. **26**, 745–748 (2003). https://doi.org/10.1023/A:1020706423230

62. N. Özer, F. Tepehan, Optical and electrochemical characteristics of sol–gel deposited iron oxide films. Sol. Energy Mater. Sol. Cells **56**, 141–152 (1999). https://doi.org/10.1016/S0927-0248(98)00152-4

63. G. Zotti, G. Schiavon, S. Zecchin, U. Casellato, Electrodeposition of amorphous Fe2O3 films by reduction of iron perchlorate in acetonitrile. J. Electrochem. Soc. **145**, 385–389 (1998). https://doi.org/10.1149/1.1838273

64. M.F. Al-Kuhaili, M. Saleem, S.M.A. Durrani, Optical properties of iron oxide (α-Fe2O3) thin films deposited by the reactive evaporation of iron. J. Alloys Compd. **521**, 178–182 (2012). https://doi.org/10.1016/j.jallcom.2012.01.115

65. L. Dghoughi, B. Elidrissi, C. Bernède, M. Addou, M.A. Lamrani, M. Regragui, H. Erguig, Physico-chemical, optical and electrochemical properties of iron oxide thin films prepared by spray pyrolysis. Appl. Surf. Sci. **253**, 1823–1829 (2006). https://doi.org/10.1016/j.apsusc.2006.03.021

66. G.B. Sakura, A.Y.T. Leung, Experimental study of particle collection efficiency of cylindrical inlet type cyclone separator. Int. J. Environ. Sci. Dev. **6**, 160–164 (2015). https://doi.org/10.7763/ijesd.2015.v6.581

67. N. Izza, S.R. Dewi, A. Setyanda, A. Sukoyo, P. Utoro, D.F. Al Riza, Y. Wibisono, Microwave-assisted extraction of phenolic compounds from *Moringa oleifera* seed as anti-biofouling agents in membrane processes. MATEC Web Conf. **204**, 03003–03009 (2018). https://doi.org/10.1051/matecconf/201820403003

68. O.S. Bello, K.A. Adegoke, O.O. Akinyunni, Preparation and characterization of a novel adsorbent from *Moringa oleifera* leaf. Appl. Water Sci. **7**, 1295–1305 (2017). https://doi.org/10.1007/s13201-015-0345-4

69. C.S.T. Araújo, E.I. Melo, V.N. Alves, N.M.M. Coelho, *Moringa oleifera* Lam. seeds as a natural solid adsorbent for removal of AgI in aqueous solutions. J. Braz. Chem. Soc. **21**, 1727–1732 (2010). https://doi.org/10.1590/S0103-50532010000900019

70. S. Kanagasubbulakshmi, K. Kadirvelu, Green synthesis of iron oxide nanoparticles using *Lagenaria siceraria* and evaluation of its antimicrobial activity. Def. Life Sci. J. **2**, 422–427 (2017). https://doi.org/10.14429/dlsj.2.12277

71. N. Maroofpour, M. Alizadeh, M. Hatami, B. Asgari Lajayer, Biological synthesis of nanoparticles by different groups of bacteria, in *Microbial Nanobionics*. (Springer, Cham, 2019), pp. 63–85

72. I. Abdulkadir, H.M.I. Abdallah, S.B. Jonnalagadda, B.S. Martincigh, The effect of synthesis method on the structure, and magnetic and photocatalytic properties of hematite (α-Fe2O3) nanoparticles—research article. S. Afr. J. Chem. **71**, 68–78 (2018). https://doi.org/10.17159/0379-4350/2018/v71a9

73. J. Vidal-Vidal, J. Rivas, M.A. López-Quintela, Synthesis of monodisperse maghemite nanoparticles by the microemulsion method.

74. Colloids Surf. A **288**, 44–51 (2006). https://doi.org/10.1016/j.colsurfa.2006.04.027

74. D.M. Yufanyi, A.M. Ondoh, J. Foba-Tendo, K.J. Mbadcam, Effect of decomposition temperature on the crystallinity of α-Fe 2 O 3 (hematite) obtained from an iron(III)-hexamethylenetetramine precursor. Am. J. Chem. **5**, 1–9 (2015). https://doi.org/10.5923/j.chemistry.20150501.01

75. E. Darezereshki, F. Bakhtiari, M. Alizadeh, A. Behrad vakylabad, M. Ranjbar, Direct thermal decomposition synthesis and characterization of hematite (α-Fe2O3) nanoparticles. Mater. Sci. Semicond. Process. **15**, 91–97 (2012). https://doi.org/10.1016/j.mssp.2011.09.009

76. S. Ahmadi, L. Mohammadi, C.A. Igwegbe, S. Rahdar, A.M. Banach, Application of response surface methodology in the degradation of reactive blue 19 using H2O2/MgO nanoparticles advanced oxidation process. Int. J. Ind. Chem. **9**, 241–253 (2018). https://doi.org/10.1007/s40090-018-0153-4

77. D.C. Montgomery, *Design and Analysis of Experiments* (Wiley, Hoboken, 2017)

78. C.A. Igwegbe, L. Mohmmadi, S. Ahmadi, A. Rahdar, D. Khadkhodaiy, R. Dehghani, S. Rahdar, Modeling of adsorption of Methylene Blue dye on Ho-CaWO4 nanoparticles using response surface methodology (RSM) and artificial neural network (ANN) techniques. MethodsX **6**, 1779–1797 (2019). https://doi.org/10.1016/j.mex.2019.07.016

79. E.K. Tetteh, S. Rathilal, M.N. Chollom, Pre-Treatment of industrial mineral oil wastewater using response surface methodology. WIT Trans. Ecol. Environ. **216**, 181–191 (2017). https://doi.org/10.2495/WS170171

80. M. Sarkar, P. Majumdar, Application of response surface methodology for optimization of heavy metal biosorption using surfactant modified chitosan bead. Chem. Eng. J. **175**, 376–387 (2011). https://doi.org/10.1016/j.cej.2011.09.125

81. D.F. Swinehart, The Beer-Lambert law. J. Chem. Educ. **39**, 333–335 (1962). https://doi.org/10.1021/ed039p333

82. C. Moya, X. Batlle, A. Labarta, The effect of oleic acid on the synthesis of Fe3-xO4 nanoparticles over a wide size range. Phys. Chem. Chem. Phys. **17**, 27373–27379 (2015). https://doi.org/10.1039/c5cp03395k

83. J. Cao, Y. Wu, Y. Jin, P. Yilihan, W. Huang, Response surface methodology approach for optimization of the removal of chromium(VI) by NH2-MCM-41. J. Taiwan Inst. Chem. Eng. **45**, 860–868 (2014). https://doi.org/10.1016/j.jtice.2013.09.011

84. Y.-N. Chang, M. Zhang, L. Xia, J. Zhang, G. Xing, The toxic effects and mechanisms of CuO and ZnO nanoparticles. Materials (2012). https://doi.org/10.3390/ma5122850

85. W. Ahmad, K. Kumar Jaiswal, M. Amjad, *Euphorbia herita* leaf extract as a reducing agent in a facile green synthesis of iron oxide nanoparticles and antimicrobial activity evaluation. Inorg. Nano-Metal Chem. **51**, 1147–1154 (2021). https://doi.org/10.1080/24701556.2020.1815062

86. W. Ahmad, K.K. Jaiswal, S. Soni, Green synthesis of titanium dioxide (TiO2) nanoparticles by using *Mentha arvensis* leaves extract and its antimicrobial properties. Inorg. Nano-Metal Chem. **50**, 1032–1038 (2020). https://doi.org/10.1080/24701556.2020.1732419

87. V.V.T. Padil, M. Černík, Green synthesis of copper oxide nanoparticles using gum karaya as a biotemplate and their antibacterial application. Int. J. Nanomed. **8**, 889 (2013)

88. X. Liang, M. Sun, L. Li, R. Qiao, K. Chen, Q. Xiao, F. Xu, Preparation and antibacterial activities of polyaniline/Cu 0.05Zn 0.95O nanocomposites. Dalt. Trans. **41**, 2804–2811 (2012). https://doi.org/10.1039/c2dt11823h

89. O. Amadine, Y. Essamlali, A. Fihri, M. Larzek, M. Zahouily, Effect of calcination temperature on the structure and catalytic performance of copper–ceria mixed oxide catalysts in phenol

hydroxylation. RSC Adv. **7**, 12586–12597 (2017). https://doi.org/10.1039/C7RA00734E

90. I.P.T. Indrayana, L.A. Tjuana, M.T. Tuny, Nanostructure and optical properties of Fe 3 O 4: effect of calcination temperature and dwelling time. J. Phys. Conf. Ser. **1341**, 082044–082053 (2019). https://doi.org/10.1088/1742-6596/1341/8/082044

91. C.-C. Diao, C.-Y. Huang, C.-F. Yang, C.-C. Wu, Morphological, optical, and electrical properties of p-type nickel oxide thin films by nonvacuum deposition. Nanomaterials **10**, 636–651 (2020). https://doi.org/10.3390/nano10040636

92. F.N. Sayed, V. Polshettiwar, Facile and sustainable synthesis of shaped iron oxide nanoparticles: effect of iron precursor salts on the shapes of iron oxides. Sci. Rep. **5**, 9733–9747 (2015). https://doi.org/10.1038/srep09733

93. P. Rajiv, B. Bavadharani, M.N. Kumar, P. Vanathi, Synthesis and characterization of biogenic iron oxide nanoparticles using green chemistry approach and evaluating their biological activities. Biocatal. Agric. Biotechnol. **12**, 45–49 (2017). https://doi.org/10.1016/j.bcab.2017.08.015

94. S.S.U. Rahman, M.T. Qureshi, K. Sultana, W. Rehman, M.Y. Khan, M.H. Asif, M. Farooq, N. Sultana, Single step growth of iron oxide nanoparticles and their use as glucose biosensor. Results Phys. **7**, 4451–4456 (2017). https://doi.org/10.1016/j.rinp.2017.11.001